Die approbierte Originalversion dieser Diplom-/Masterarbeit ist in der Hauptbibliothek der Technischen Universität Wien aufgestellt und zugänglich.
http://www.ub.tuwien.ac.at

TECHNISCHE UNIVERSITÄT WIEN

The approved original version of this diploma or master thesis is available at the main library of the Vienna University of Technology.
http://www.ub.tuwien.ac.at/eng

DIPLOMARBEIT

Analyzing spatial organization and clustering of the T cell receptor

zur Erlangung des akademischen Grades

Diplom-Ingenieur

im Rahmen des Studiums

Biomedical Engineering

eingereicht von

Bernd Reutterer, BSc
Matrikelnummer 01329074

ausgeführt am Institut für Angewandte Physik
der Fakultät für Physik der Technischen Universität Wien
(in Zusammenarbeit mit XYZ)

Betreuung
Betreuer/in: Univ.Prof. Dipl.-Ing. Dr.techn. Gerhard Schütz
Betreuer/in: Dr. Florian Baumgart

Wien, 28.11.2018

(Unterschrift Verfasser/in)

(Unterschrift Betreuer/in)

Abstract

The spatial organization of proteins and lipids within the cell membrane is of high interest as it is thought to regulate cell signaling. The formation of T cell receptor (TCR) microclusters and the immunological synapse upon T cell activation was key to realize that the orchestrated spatial rearrangement of T cell signaling proteins was important for T cell function. After development of single molecule localization microscopy methods like PALM and (d)STORM, results suggesting the nanoscale clustering of membrane proteins were published. Importantly, nanoclusters of the TCR were found even in non-activated T cells. However, recent findings indicate that fluorophore blinking could lead to overcounting and therefore to the erroneous detection of (non-existing) nanocluster. This thesis applies a novel experimental strategy to overcome these blinking effects. The method relies on the principle of labeling the same protein with two different fluorophores. Clustered and randomly distributed proteins can be discriminated by characteristically different distance distributions of the localizations between the two color channel. The technique was used in activated and nonactivated primary mouse T cells to investigate the spatial organization of the T cell receptor. Results show a clear differennce for non-activated and activated T cells. In addition to investigating the nanoscale organization of the TCR, the role of intracellular structures (e.g. endoplasmic reticulum (ER)) in influencing the spatial distribution of TCR microclusters upon T cells activation was addressed. The ER is known to bind to the plasma membrane upon T cell activation to facilitate the inflow of Ca^{2+} from the extracellular space into the cell. Two color fluorescence imaging was used to test whether the spatial organization of the TCR depends on the position of ER-plasma membrane junctions.

Kurzfassung

Die räumliche Verteilung von Proteinen und Lipiden der Plasmamembran ist von großem wissenschaftlichem Interesse, da diese für die Signalweiterleitung innerhalb der Zelle als bedeutend gilt. Ein bekanntes Beispiel von struktureller Organisation von Membranproteinen ist die Formation von Mikroclustern und der Immunologischen Synapse in Folge der Aktivierung von T Zellen. Hochauflösende Messmethoden in der Mikroskopie wie PALM oder (d)STORM zeigten, dass Membranproteine, wie auch der T Zell Rezeptor, in noch kleineren Clustern im Nanometerbereich organsiert sind. Jüngste Erkenntnisse über Artefakte, die beim Messen mit solchen Methoden auftreten, wecken jedoch Zweifel an diesen Ergebnissen. Die verwendeten Messmethoden beruhen auf dem Blinken von Fluorophoren, was dazu führen kann, dass ein und dasselbe Fluorophor öfters detektiert und als Cluster interpretiert wird. In dieser Arbeit wird eine Methode, die von diesem Effekt nicht betroffen ist erstmals angewendet. Bei dieser Methode wird ein Protein mit zwei verschiedenen Farbstoffen markiert und die Distanzen zwischen einer Lokalisation und dem nächsten Nachbaren im zweiten Farbkanal berechnet. Durch einen Unterschied zwischen den Verteilungen der Distanzen im Fall eines geclusterten Moleküls und einer Zufallsverteilung der Proteine kann man Cluster detektieren. In dieser Arbeit wurde diese Methode zur Untersuchung der räumlichen Organisation des T Zell Rezeptors in aktivierten und nicht-aktivierten Maus-T Zellen verwendet. Die Ergebnisse weisen einen klaren Unterschied für nicht-aktivierte und aktivierte T Zellen auf. Des Weiteren wurde untersucht, ob die räumliche Anordnung von T Zell Rezeptor Microclustern in der T Zell Plasmamembran von der Position des Endoplasmatischen Retikulums abhängig sind, da dieses laut Literatur nach der Aktivierung einer T Zelle and die Plasmamembran bindet um einen Ca^{2+} Einstrom in die Zelle zu ermöglichen.

Acknowledgments

I want thank Prof. Gerhard Schütz, who sparked my interest for the field of biophysics, especially for single molecule microscopy and who gave me the opportunity to conduct this study in his research group.
Additionally, I want to thank Dr. Florian Baumgart for his supervision during this thesis and the prior project work. It was a great pleasure to work with him on the different projects and discuss results and further approaches.
I also want to thank Karoline Pill and my family for always supporting me during this master study program, especially during stressful periods of exams or writing this thesis.

Table of Contents

List of Figures

List of Tables

List of Abbrevations

Abbrevation	Definition
(d)STORM	(direct) Stochastic Optical Reconstruction Microscopy
AOM	acousto-optic modulators
APC	Antigen presenting cell
BSA	Bovine serum albumin
CCD	Charged-coupled device
CRAC	Calcium relese activated calcium
c-SMAC	central supra-molecular activation cluster
DAG	diacylglyerol
ER	Endoplasmic reticulum
FBS	Fetal bovine serum
GA	Glutaraldehyde
IP_3	inositol 1,4,5-triphosphate
IS	Immunological synapse
ITAM	immune-receptor tyrosine-based activation motif
LAT	linker of activated T cells
Lck	lymphocyte-specific protein tyrosine kinase
NFAT	Nucelar factor of activated T cells
NTA	Nitrilotriacetic acid
PALM	Photoactivated Localization Microscopy
PFA	Paraformaldehyde
PLC-γ	phospholipase C-γ
POPC	1-palmitoyl-2oleoyl-sn-glycerol-3-phosphocholine
PSF	Point spread function
p-SMAC	peripheral supra-molecular activation cluster
ROI	Region of interest
SLB	Supported lipid bilayer
SLP-67	lymphocyte cytosolic protein 2

SMLM	single molecule localization microscopy
STIM1	stromal interaction molecule 1
TCR	T cell receptor
TIRF	Total Internal Reflection Fluorescence Microscopy
ZAP-70	zeta-chain-associated protein kinase 70

List of Symbols

Symbol	Definition
b	Distance of the intermediate image
B_1	Intermediate image
CV	Coefficient of variation
$f(r)$	Probability distribution function
F_1	Focal plane of objective
F_2	Focal plane of eyepiece
F_D	Cumulative distribution function
F_T	Focal plane of tube lens
G	Object
g	Distance of the object
$\bar{I}$	Mean intensity
k_{isc}	Intersystem crossing rate
k_{red}	Reduction rate
L_1	Objective lens
L_2	Eyepiece lens
L_T	Tube lens
M_{OB}	Magnification of objective
M_{OK}	Magnification of eyepiece
n	Refractive index
NA	Numerical aperature
$S^{\bullet}$	Dye radical
S_0	Ground state
S_1	First Excited state
SH	Fully reduced dye
T_1, T_2	Triplet states
α	Opening angle of the objective
δ	Distance between object and focal plane of objective

η	Area of cluster
$\theta_{critical}$	Critical angle of total reflection
λ	Wavelength
ρ	Localization density inside cluster
σ	Standard deviation

1. Introduction

The study of cells began with the development of microscopes and until now, light microscopy in its various forms is a key tool of biological research [1]. The transparent appearance of cells makes it hard to investigate cell structures by using brightfield microscopy. The development of fluorescence microscopy made it possible to label specific molecules of interest with a fluorescent dye, which emits light of a certain wavelength, upon absorption of light with a shorter wavelength [2]. However, even if standard fluorescence microscopy facilitates the study of internal cell structures, its resolving power is limited by the diffraction limit of light. Within the last decade super resolution fluorescence microscopy methods, which are based on the exact localization of individual fluorophores, were developed. These methods achieve a resolution of about 20 nm, which is about a tenth of the diffraction limit [3]. Effects of membrane compartmentalization were already studied with standard fluorescence microscopy. A prominent example is the formation of microclusters of T cell receptors upon T cell activation. After development of super resolution microscopy techniques, experiments were published suggesting the existence of even smaller protein clusters, called nanoclusters. Nanoclustering was found for almost every membrane protein, even for the TCR in non-activated T cells. A suggested advantage for clustered membrane proteins in immune cells is the increased sensitivity due to the higher probability of rebinding [4]. However, recent findings point out that these apparent clusters are most likely artifacts inherent to superresolution techniques, because blinking of the fluorophores lead to overcounting of single dye molecules and the detection of clusters [5]. Some methods tried to get rid of these artifacts by analytical means. However, it is hard to distinguish between overcounting due to blinking of one fluorophore and signals from multiple emitters within a real cluster. The future goal is to develop experimental approaches which are insensitive to the mentioned artefacts. Baumgart et al. developed a method which works by using different labeling densities for one protein. By analyzing the density of detected localizations within appearing localization clusters and the area of these clusters, real protein clusters can be distinguished from random distributions of proteins [6]. The method used in this work relies on the principle of labeling the same protein with two different fluorophores. Clustered and randomly distributed proteins can be discriminated by characteristically different distance distributions of the localizations between the two color channel [7].

1.1. Light Microscopy

The ability of microscopes to visualize cells and their internal structures makes optical microscopy a key tool in biological research [8]. A simple representation of a light microscope is shown in **Figure 1**. The depicted setup consists of two lenses, L_1 and L_2, which are called objective and eyepiece. The objective L_1 projects a real and inverted image (B_1) of the object G at the front focal plane of the eyepiece. To generate a magnified intermediated image B_1, the object G needs to be placed somewhere outside the front focal plane F_1 of the objective. Since the intermediate image B_1 is located in the focal plane of the eyepiece, the eyepiece acts as magnifying glass and produces a virtual image at infinity, which can be viewed [9].

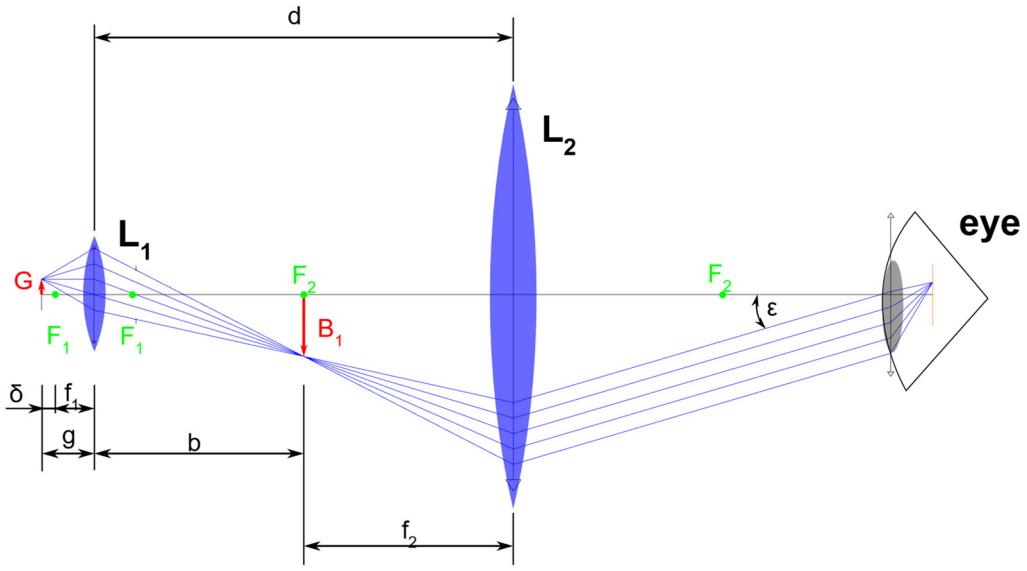

Figure 1: Simple schematic of a microscope, consisting of two lenses, the objective (L_1) and the eyepiece (L_2). The objective generates a magnified, real but inverted image of the object, whereas L_2 acts as magnifying glass and produces a virtual image at infinity

The magnification of the setup in **Figure 1** can be calculated by multiplying the magnification of the objective (M_{OB}) with the magnification of the eyepiece (M_{OK}). M_{OB} is calculated by dividing the distance b between the intermediate image and L_1 by the distance g of the object to L_1 (**Formula 1**). If the specimen is placed near the focal plane F_1, g can be replaced by f_1. M_{OK} is given by the magnification of a magnifying glass in case that the object is placed at the focal plane, whereas s_0 is called the near distance of the eye and defined as 25 cm for humans (**Formula 2**). An object placed closer than these 25 cm to the cannot be seen sharp by the human eye because the accommodation power of the eye lens is to low. **Formula 3** depicts the overall magnification of a microscope [9].

$$M_{OB} = \frac{b}{g} = \frac{d - f_2}{g} \qquad (1)$$

$$M_{OK} = \frac{s_0}{f_2} \qquad (2)$$

$$M = M_{OB} \cdot M_{OK} = \frac{(d - f_2) \cdot s_0}{g \cdot f_2} \approx \frac{(d - f_2) \cdot s_0}{f_1 \cdot f_2} \qquad (3)$$

Modern objectives are built in a way that is called infinity-corrected. This principle of an additional tube lens placed between objective lens and eyepiece is shown in **Figure 2**. Placing the object in the front focal plane of lens L_1 leads to parallel rays between L_1 and the tube lens L_T. The intermediate image is formed in the back focal plane of the tube lens which is also the front focal plane of the eyepiece. The advantage of this system containing a space with parallel light rays is, that optical components like filters can be placed there, without that their optical imperfections or dirt is visible at the image plane [2].

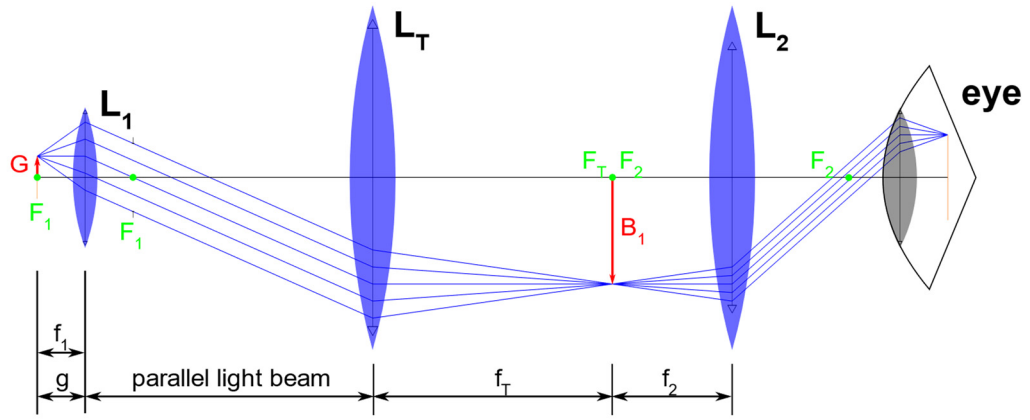

Figure 2: Infinity corrected microscope setup. By adding an additional lens L_T (tube lens) between the objective L_1 and the eyepiece L_2 the object can be place in the front focal plane of L_1. This leads to parallel rays between L_1 and L_T. Between these two lenses, additional filters can be placed, without their optical imperfections distorting the image.

Importantly, in modern microscopy systems charged-coupled device (CCD) cameras are used as detectors. These devices are placed in the intermediate image plane between the tube lens and the eyepiece [2].

Using classic brightfield microscopy, a specimen generates an image due to absorption and scattering of light when illuminated by a light source placed on the opposite side as the sensor. Biological samples like cells are generally thin and transparent, and therefore lead to a low

contrast when using brightfield microscopy [2] [8]. To overcome such contrast issues when studying cells and their internal structures, different methods like darkfield microscopy or phase contrast microscopy can be used. However, the most popular method to visualize structures of cells is to use fluorescent dyes [2] [10].

1.1.1. The Principle of Fluorescence

Fluoresce microscopy is a powerful tool to study specimens with low contrast like cells. The principle of this method is to label molecules of interest in a cell with so-called fluorophores. Fluorophores can absorb and emit light. Normally, a fluorophore is in the so-called ground state (S_0). By absorbing light of a certain wavelength, a change in its electronical, vibrational and rotational states can occur. This process can lead to a transition from the ground state to one of a number of excited states (for example S_1). Physically, this means that one of the outermost electrons is moved to another orbital with higher distance to the nucleus and therefore higher energy level. After a certain time, the molecule falls back to its ground state, emitting a photon. In general, the wavelength of the emitted light is longer, i.e. of lower energy, than the wavelength of the absorbed light. This phenomenon is called stokes shift. The stokes shift occurs because some energy is stored as vibrational energy, which dissipates because of vibrational relaxation. This leads to the effect, that the molecule has the lowest possible energy level of the exited state S_1. From this level, the transition to the ground state occurs and light is emitted. From the lowest energy level of S_1, the fluorophore can reach different vibrational levels of the ground state, which means different energy levels. This leads to the fact that not only one wavelength is possible for the emitted light, but a whole spectrum. By using Jablonski diagrams, like shown in **Figure 3**, energy levels and transitions between them can be represented.

The diagram in **Figure 3** shows different singlet energy states, S_0, S_1 and S_2. Furthermore, two so-called triplet states T_1 and T_2 are shown. When electrons are transferred into another singlet state, their spin of +1/2 or -1/2 is conserved and it stays antiparallel to the spin of the second electron of its original orbital. However, an excited electron can also undergo intersystem crossing, although with a very low probability. This means that the electron flips its spin and reaches one of the shown triplet states. A transition to the original ground state is possible, but due to the fact that the electron needs to flip its spin again the probability is again rather small. Therefore, this process takes longer than transitions from a higher singlet state to the ground state [2] [10].

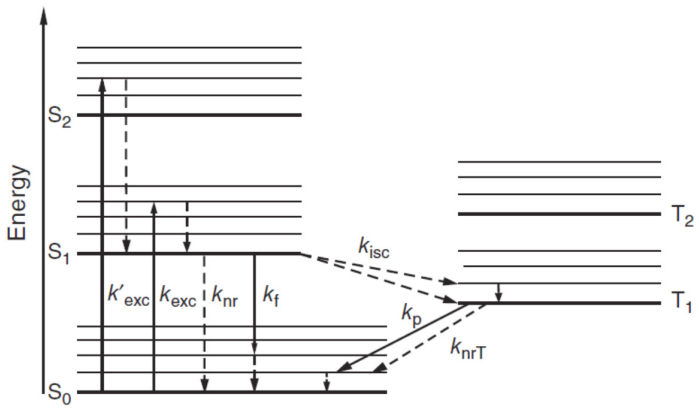

Figure 3: Jablonski diagram showing different energy levels and transitions between them. On the left side the singlet states S_0, S_1 and S_2 are shown. On the right side triplet states are shown. Every state has sub-energy levels, which exist due to different vibrational and rotational energies. Figure adapted from Kubitschek [2].

The absorption and emission spectra and the corresponding energy levels of the common fluorophore FITC are displayed in **Figure 4**. The overlap of absorption and emission spectrum is explained by the fact that the molecule can be in a higher vibrational energy state of the ground state before absorption than after the emission. This leads to the emission of light with higher energy. The stokes shift and the overlap of absorption and emission spectra depends on the fluorophore itself [10].

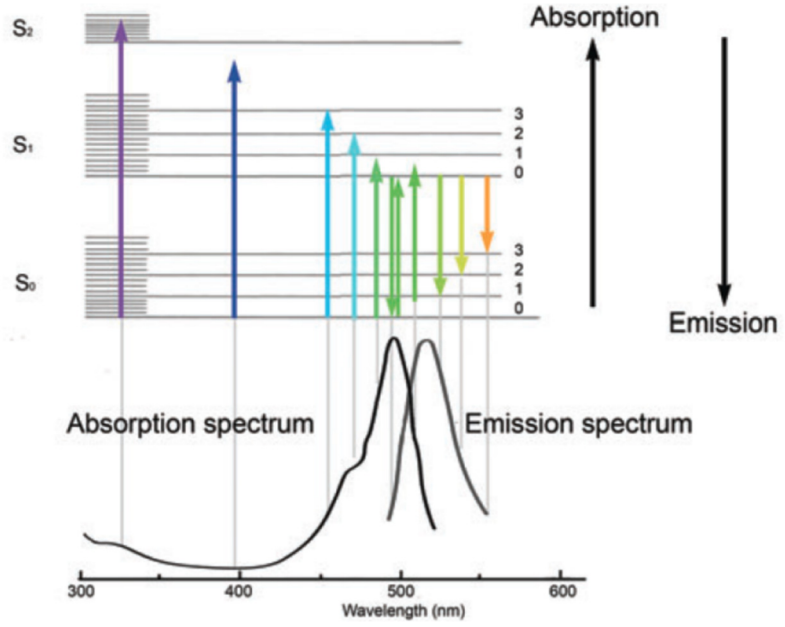

Figure 4: Absorption and emission spectra of the fluorophore FITC. The upper part shows possible transitions between the ground state S_0 and the excited states S_1 and S_2. The color of the arrows depicts the wavelength and therefore also the energy of the absorbed or emitted light. Stokes shift and overlap between absorption and emission spectra can be clearly seen. Figure adapted from Lichtman et al. [10].

1.1.2. Fluorescence Microscopy

The basic construction principle of a fluorescence microscope is shown in **Figure 5**. Most setups are used in epi-illumination mode, meaning that the objective is used for collecting light from the specimen and for magnifying it, but is also used for illumination of the object. This method has the advantage that the part of the excitation light which runs from the specimen to the camera is very small and only depends on the emission from the object. Due to the stokes shift and by using special filters it is possible to split up the excitation light and the light which is emitted by the fluorophore. Such filter systems are normally placed between objective and tube lens taking advantage of parallel rays. In the setup in **Figure 5** the filter composition consists of an excitation filter (2), a dichroic mirror (3) and an emission filter (4). The excitation filter only transmits wavelengths which are needed for excitation of the used fluorophores. The emission filter is placed within the imaging path, before the camera, and only transmits light within the emission range of the fluorophore. The dichroic mirror reflects light below a certain wavelength and transmits light above this wavelength. This cut-off wavelength should be near the intersection between the absorption and emission spectrum of the used fluorophore. A filter cube setup with the bandwidth diagrams of the single components is illustrated in **Figure 6** [2] [10].

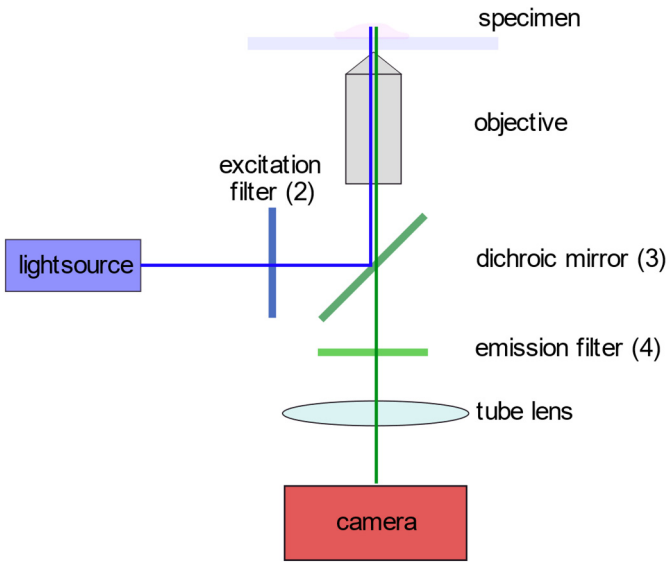

Figure 5: Setup of a simple fluorescence microscope. The objective is used to illuminate the sample and to collect the photons emitted by the fluorophores. Due to the stokes shift and an appropriate filter set it is possible to separate the emitted light from the excitation light.

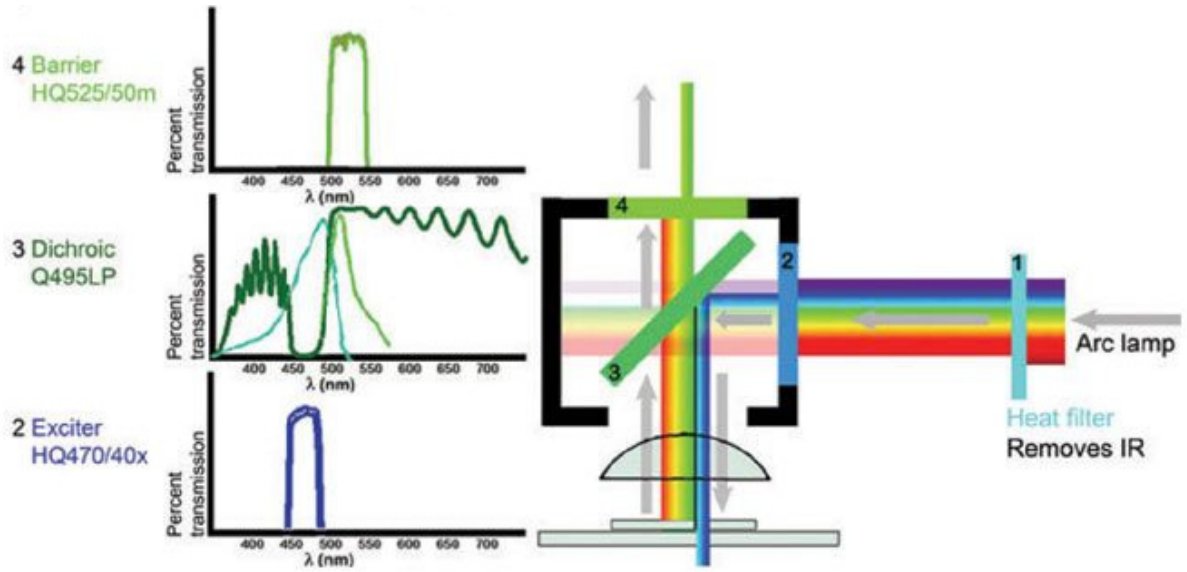

Figure 6: Detailed illustration of the filter setup within a fluorescence microscope, showing excitation filter (2), dichroic mirror (3), emission filter (4) and the bandwidth diagrams of these components. Figure adapted from Lichtman et al. [10].

Even though fluorescence microscopy is a very prominent tool in biology, its resolution is limited by the diffraction limit of the used light [11] [12]. **Formula 4** gives the minimal distance between two objects that can be resolved according to Ernst Abbe, where NA is the numerical aperture of the objective. NA is given by multiplying the refractive index between specimen and objective (n) by half of the opening angle (α) of the objective [3].

$$x = \frac{\lambda}{2 \cdot NA} = \frac{\lambda}{2 \cdot n \cdot \sin(\alpha)} \qquad (4)$$

Using for example green light with a wavelength of 550 nm and an oil immersion objective with a numerical aperture of 1.46, the minimal distance of two resolvable point emitters would be about 188 nm. Comparing this value with the size of cells and internal structures of a cell gives information which structures can be analyzed by standard light microscopy. The diameter of a typical animal cells is about 20 µm, which is about 100 times the resolution limit. Organelles like mitochondria are about 2 µm in diameter, which is also above the resolution limit. However, other internal structures like ribosomes or single molecules have sizes of a few nm, which is at least an order of magnitude below the resolution limit of a standard light microscope and cannot be analyzed with it [1]. **Figure 7** gives an overview of the resolution power of light microscopes and the size of different structures of a typical cell.

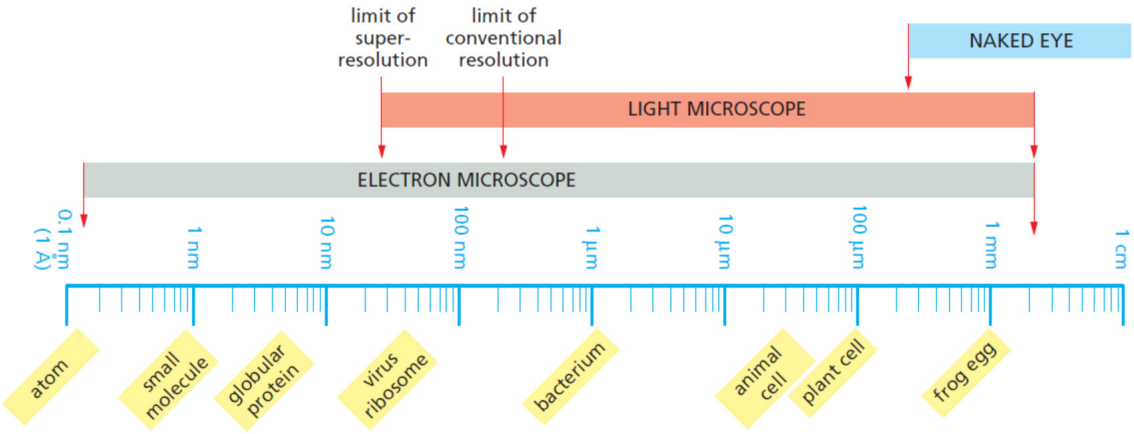

Figure 7: Resolution power of a microscope in comparison with the size of different cell types and internal structures. Figure adapted from Alberts [1].

1.1.3. Superresolution microscopy

In order to study proteins inside the cell or its membrane at the single molecule level, the resolution power of a standard fluorescence microscope is insufficient. **Formula 4** shows that decreasing the wavelength would increase the resolution capability. A method which provides a better resolution is electron microscopy [3]. For this technique electrons are accelerated by voltages in the kV range which leads to corresponding de Broglie wavelengths below 0.01 nm [13] . However, factors like sample preparation, conditions for the sample during imaging and interaction between the electron and the sample make it difficult to use electron microscopy in biology [3] [14], particularly in live samples.

The first developed methods allowing a resolution below the diffraction limit for optical microscopy utilize special illumination techniques, like structured illumination microscopy [15] or stimulated emission depletion fluorescence microscopy [16]. A second group of superresolution microscopy methods exploits the fact that the position of an individual fluorophore signal can be determined with nm-precision. The methods Photoactivated Localization Microscopy (PALM) [17] or (direct) Stochastic Optical Reconstruction Microscopy (dSTORM) [11] [12] belong to this group of superresolution imaging techniques [12] [3].

In this thesis project dSTORM was used to image membrane proteins, therefore the (d)STORM method is described in more detail.

1.1.4. (direct) Stochastic Optical Reconstruction Microscopy

STORM is based on the fact that it is possible to determine the position of a single fluorophore with very high precision. This can be done by fitting a gaussian function to the measured Point Spread Function (PSF) of the fluorophore. Rust et al. measured the position of single fluorophores numerous times and determined a localization accuracy of about 20 nm [11]. To use this localization method for super resolution microscopy it is important that two bright fluorophores are separated by a minimal distance of the diffraction limit. By using this setup, the position of these individual fluorophores can be determined. STORM microscopy uses fluorophores with so-called dark states also called OFF states. When a fluorophore is excited and emits light it is in the ON state. At every timepoint during a STORM imaging sequence only a small number of fluorophores is in ON state. After an image is taken a different set of fluorophores is switched into the ON state and another image is taken. As long as the distance between two active fluorophores is higher than the diffraction limit at every time-point t, the position of the fluorophores can be determined exactly. By using all images of the sequence and overlaying them, the structure can be reconstructed with a resolution below the diffraction limit [11][12]. In the first implementation of the STORM principle, Rust et al. used two cyanine dyes Cy 3 and Cy5 located in close proximity to each other. By using a red laser, the Cy5 dye is excited and emits light but can also be brought into a stable dark state. Using a green laser, the Cy5 dye can be brought back into a fluorescence state. For analyzing a sample, they used a measurement sequence shown in **Figure 8**. At first a strong red laser impulse converted all fluorophores into a dark state. Then by using a green laser, a random small fraction of dyes was brought back into the ON state and then was imaged with the red laser and again converted into a dark state. With the green laser another fraction was converted into the fluorescence state [11].

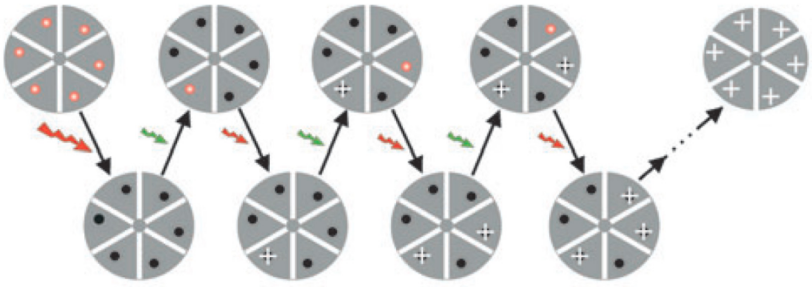

Figure 8: Sequence for a typical STORM experiment. By using a red and a green laser only a small fraction of fluorophores is switched into the fluorescent state at a certain timepoint and imaged. The position of one fluorophore can be determined with high accuracy. Overlaying the localization maps of single images leads to a localization map of all molecules in the sample with a resolution below the diffraction limit. Figure adapted from Rust et al. [11].

In contrast to the method used by Rust *et al.*, direct Stochastic Optical Reconstruction Microscopy (dSTORM) does not use a fluorophore pair. Instead, conventional fluorescent probes in an aqueous buffer with a millimolar concentration of reducing thiols is used. Using appropriate wavelengths for illumination, switching between a fluorescent ON-state and a non-fluorescent OFF state is achieved. Such induced switching cycles are illustrated in **Figure 9**. It is shown that the dye can be excited upon radiation into the singlet state S_1 and falls back into its ground state by emitting light. With a certain rate k_{isc} an intersystem crossing to the triplet state ^3S is possible. In the presence of millimolar concentrations of thiols this triplet state can be reduced with the rate k^1_{red}. Thereby a dye radical $S^\bullet$ and a thiol radical are formed. The $S^\bullet$ form of ATTO dyes can accept another electron forming a fully reduced dye SH. By oxidation of the triplet state or any of its reduced versions during irradiation with light of about 400 nm the original ground state can be restored. This cycle happens several times until the dye undergoes photobleaching. By varying laser power and concentration of the buffer, the ON and OFF rates of the dye can be manipulated. This makes it possible to adjust the amount of simultaneously active fluorophores [12] [18].

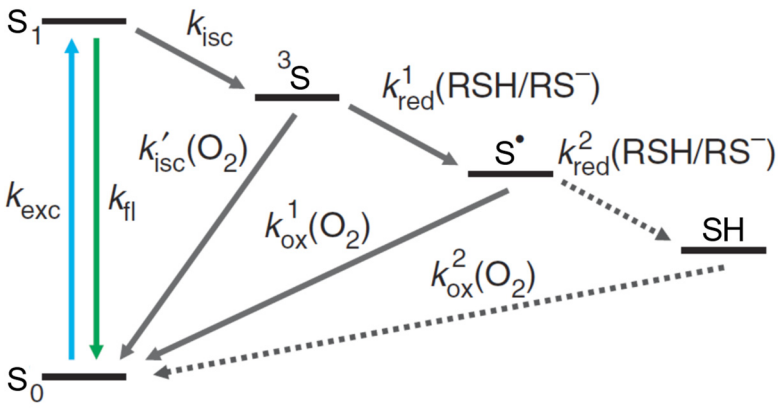

Figure 9: Photoswitching example of Alexa Fluor and ATTO dyes in aqueous buffers with millimolar thiol concentrations. The triplet state of the fluorophore is reduced by these thiols and the formation of a dye radical anion and a thiyl radical happens. By using a laser in the UV range (about 400 nm) and due to oxidation, the dye can be switched back into its fluorescence state. Figure adapted from van de Linde et al. [12].

To study different cellular structures or proteins simultaneously, multi-color fluorescence microscopy is used. Shortly after the STORM and dSTORM techniques were published, the methods were also used with two colors. For classical STORM, one approach is using two different activator dyes and one reporter dye. In this case the color is determined by the activating laser wavelength. The second approach used two different reporter dyes coupled to

one or two activator dyes. The multi-color version for dSTORM uses two different photoswitchable dyes. Problems of two-color dSTORM can arise due to the different duty cycle and brightness of the various dyes [19]. Many of these problems appear due to different requirements concerning the buffer composition. While dyes like Alexa Fluor 647 work particularly fine in oxygen-free buffer solution, dyes with different molecular structures (e.g.: Alexa Fluor 488) show no appropriate blinking in such buffers. Nahidiazar et al. found a buffer combination, called OxEA which works for various dye combinations [20].

1.1.5. Total Internal Reflection Fluorescence Microscopy

STORM and dSTORM can be combined with Total Internal Reflection Fluorescence Microscopy (TIRF). TIRF is a microscopic method which allows that only fluorophores within 100 nm to the cover glass are illuminated and therefore excited. Implementing this method can increase the image quality due to several reasons. First, the background signal is reduced in comparison to normal epifluorescence microscopy. Second, the amount of fluorescence signal from out of focus fluorophores is reduced and the sample (living cell) is exposed to less light [21]. The method takes advantage of the physical principle of total reflection and evanescence field formation. If light is propagating from a medium with refractive index n_1 into a medium with a higher refractive index n_2, total reflection occurs if the angle with respect to the normal of the surface is bigger than the so-called critical angle $\theta_{critical}$ which can be calculated according to Formula 5 [22].

$$\theta_{critical} = \arcsin\left(\frac{n_2}{n_1}\right) \qquad (5)$$

Even if total reflection occurs, an evanescent electromagnetic field penetrates the second medium and decays exponentially with the distance to the interface of the two media. The intensity dependent on the distance z of the interface can be calculated by **Formula 6**.

$$I(z) = I_0 \cdot e^{\frac{z}{d}} \qquad (6)$$

In **Formula 6**, d is the penetration depth of the evanescent field, which is defined by **Formula 7**.

$$d = \frac{\lambda_0}{4\pi} \cdot (n_2^2 \cdot \sin^2(\theta) - n_1^2)^{-1/2} \qquad (7)$$

In Formula 7, λ0 is the wavelength in vacuum and θ the incident angle. **Formula 7** shows that increasing the incident angle θ decreases the penetration depth of the evanescent electromagnetic field.

Technically there are two methods to implement TIRF microscopy. The first technique uses a prism to direct the laser beam onto the sample. The second method makes use of objectives with a very high numerical aperture. Illumination of a small part of the back focal plane of the objective, which is near to the edge of the aperture, leads to an inclined beam and high angles at the specimen. In microscopy setups using oil immersion objectives, the refractive index of the oil matches the refractive index of glass. Therefore, light is not refracted at this interface. Total reflection takes place at the interface between the glass slice (refractive index of about 1.5) and the specimen surrounded by an aqueous buffer solution with refractive index of about 1.33 [22].

1.2. Adaptive Immunity and T cells

T lymphocytes are a specialized type of leukocytes (white blood cells), which is crucial for the adaptive immune system. T cell-mediated immune responses occur when a T cell recognizes an antigen which is presented by an antigen presenting cell (APC) via MHC complexes at the cell surface. APCs display fragments of pathogenic peptides bound to MHC molecules on the cell surface. T cells can be categorized into three types: cytotoxic T cells which directly kill an infected cell, helper T cells which stimulate the response of various other cells of the immune system like B cells or macrophages and regulatory T cells which suppress the activity of other cells of the immune system. A T cell uses a membrane complex, called the T cell receptor (TCR) for antigen recognition. The process is shown schematically in **Figure 10a**. In addition to the binding of the TCR, there are also receptors on the T cell membrane which bind to co-stimulatory proteins on the APC, as well as cell-cell adhesion proteins. Two important co-receptors are CD4 and CD8, where cytotoxic T cells are CD8 positive and helper and regulatory T cells are CD4 positive. These two co-receptors are on the one hand important to enable a sufficient binding between T cells and APCs by binding to the invariant fraction of the MHC molecule. This site is different from the TCR, which binds to the foreign peptide and the variant fraction of MHC molecule. On the other hand, CD4 and CD8 are directly involved in T cell signaling during activation. Moreover, CD4 binds to MHCII proteins whereas CD8 binds to MHCI proteins as shown in **Figure 10b**. This system ensures that one type of T cell recognizes

only a specific type of target cell, like an infected host cell in case of CD8 positive cytotoxic T cells [23].

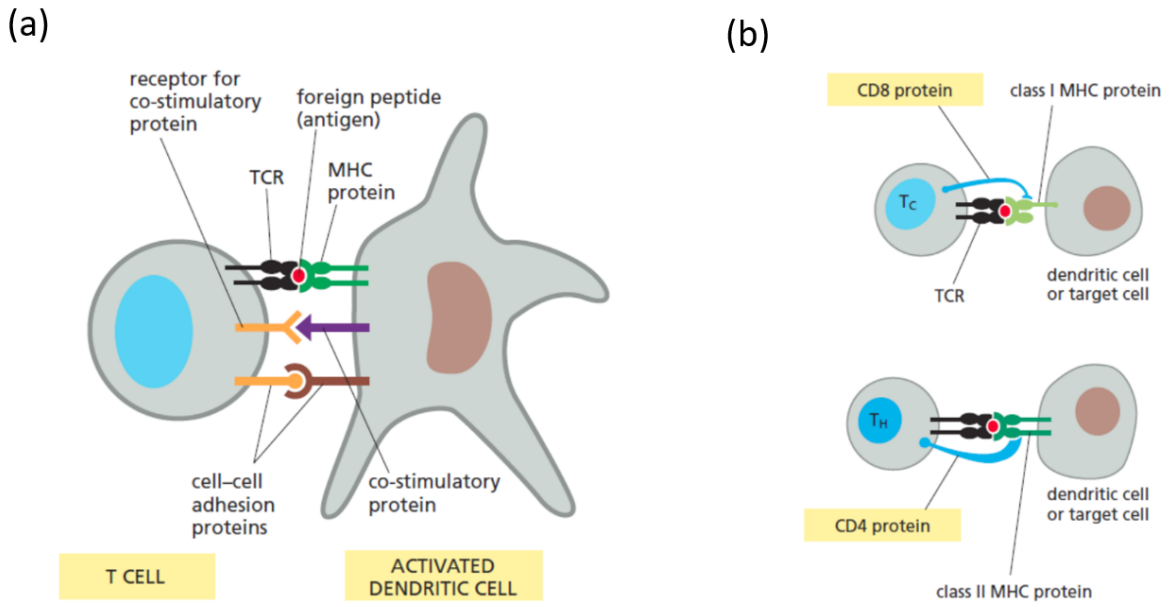

Figure 10: Overview of antigen recognition by the T cell. Panel a TCR binding to the antigenic pMHC on the surface of an APC and co-stimulatory receptors binding to co-stimulatory proteins, as well as cell-cell adhesion proteins. Panel b CD4 positive T cells bind to MHCII proteins whereas CD8 positive ones bind to MHCI proteins. Figure adapted from Alberts et al. [23].

1.2.1. T cell Maturation

The development of T cells from bone-marrow derived lymphoid progenitor cells takes place in the thymus. Due to internal signals the cells rearrange segments of the TCR gene and afterwards they express both CD4 and CD8 receptors making them CD4+/CD8+ cells. First, cells without expressing the TCR protein die by apoptosis. Afterwards, two processes called positive and negative selection determine which T cells survive and migrate. During this selection process T cells are brought in contact with MHC molecules presenting a self-peptide. T cells which do not bind to the MHC molecules fail positive selection and T cells showing a too strong recognition of self-peptides bound to a MHC fail negative selection and undergo apoptosis. On the one hand, T cells with a too high affinity for a host peptide could cause an autoimmune-disease. One the other hand, a TCR not bound to MHC presenting a peptide would have not enough sensitivity and is therefore of no value. After the initial selection process either the CD4 or the CD8 co-receptor expression is suppressed making T cells to CD4 or CD8 single-positive cells [23].

1.2.2. T cell Activation

With each TCR a so called CD3 complex is associated, which consist of two ζ chains, two ε chains, one δ chain and one γ chain. This TCR/CD3 combination, which is depicted in **Figure 11** is from now on called TCR complex. The transmembrane polypeptide chains belonging to the CD3 complex transmit an antigen recognition event by the highly invariant TCR α and β chains to an intracellular signal [23].

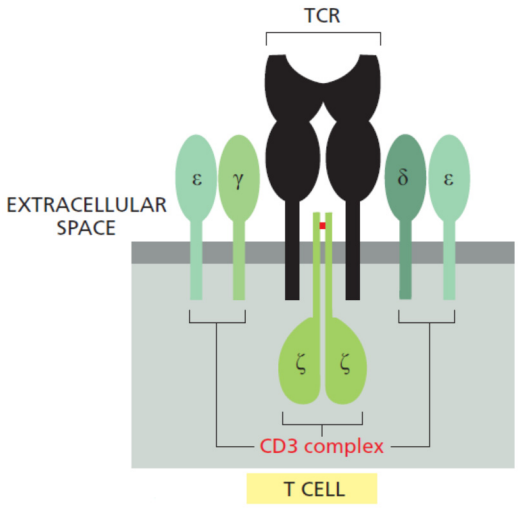

Figure 11: TCR complex, consisting of TCR α and β chains and the CD3 complex which consists of two ζ chains, two ε chains, one δ chain and one γ chain. The CD3 complex transmits the antigen recognition by the TCR to an internal cell signal. Figure adapted from Alberts et al. [23].

T cell signaling after antigen binding starts with phosphorylation of tyrosines within the cytoplasmic parts of all CD3 chains. These regions are called immune-receptor tyrosine-based activation motifs (ITAMs). In total, the TCR complex contains ten ITAMs. Upon phosphorylation by tyrosine kinases, sites for recruitment of signaling proteins are provided. Like already mentioned binding of TCR is not enough to get an adequate immune response. The important co-receptors CD4 or CD8 need to bind to the invariant part of the MHC complex. This is due to the fact that Lck, which belongs to the family of Src kinases and which is mainly responsible for ITAM phosphorylation, is associated with CD4 and CD8 inside the T cell. Due to binding of CD4 or CD8 to MHC, Lck is recruited to ITAMs. In addition, CD4/CD8 binding to MHC is considered to stabilize the TCR-peptide-MHC complex leading to enough time to generate an intracellular signal. After phosphorylation of the ITAMs, the zeta-chain-associated protein kinase 70 (ZAP-70) is recruited to the CD3ζ chain and binds to it. After this step, ZAP-70 is phosphorylated and activated by the lymphocyte-specific protein tyrosine kinase (Lck).

ZAP-70 then phosphorylates two other scaffolding proteins, which are called linker of activated T cells (LAT) and lymphocyte cytosolic protein 2 (SLP-76). This leads to the recruitment of other important signaling proteins like phospholipase C-γ (PLC-γ) to the membrane.

PLC-γ induces three different pathways important for T cell activation. The binding of PCL-γ to the plasma membrane is realized by a PH domain to a membrane lipid called PIP_3. Next PLC-γ binds to LAT and SLP-76 and is activated upon phosphorylation by the kinase ltk, which belongs to the Tec-family. Cleavage of the lipid PIP_2 by activated PLC-γ leads to two products: diacylglycerol (DAG) and inositol 1,4,5-triphosphate (IP_3). IP_3 diffuses to the endoplasmic reticulum (ER) and binds there to receptors in the ER-membrane. These receptors act as Ca^{2+} channels and are opened upon IP3 binding which leads to an efflux of Ca^{2+} from the ER into the cytosol [24]. Due to depletion of Ca^{2+} in the ER the stromal interaction molecule 1 (STIM1) within the ER membrane oligomerizes and binds to ORAI in the cell plasma membrane. This binding event opens calcium release activated channels (CRAC channels) [25]. This leads to an inflow of Ca^{2+} ions from the extracellularly space into the cell. The increase of cytoplasmic Ca^{2+} further leads to the activation of transcription factor NFAT (nuclear factor of activated T cells). The two additional pathways of T cell activation are mediated by DAG, the second product produced by PLC-γ. DAG diffuses within the plasma membrane and leads to the recruitment of protein kinase C-θ and RasGRP. Protein kinase C-θ then leads to activation of the transcription factor NFκB by activation of CARMA. RasGRP also gets activated and turns into Ras leading to activation of Fos a part of the AP-1 transcription factor. The activated transcription factors NFκB, NFAT and AP-1 then lead to specific gene transcription which starts T cell proliferation and differentiation. This whole process of T cell activation upon binding of the TCR to a foreign peptide presented by MHC is also illustrated in **Figure 12**.

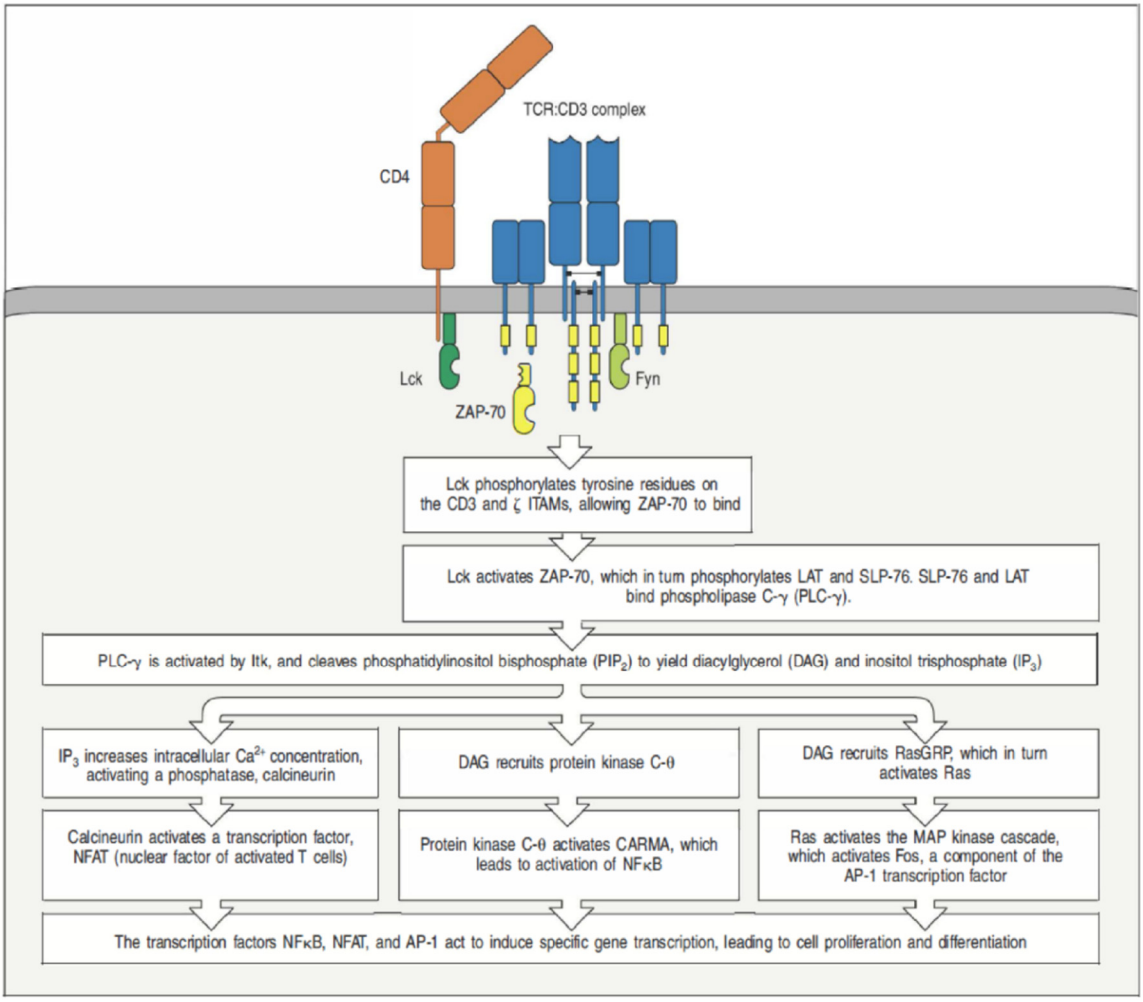

Figure 12: Overview of T cell activation after binding of the TCR and CD4 to pMHC. ITAM phosphorylation by Lck leads to the activation of ZAP-70 and the three pathways following PLC-γ activation and cleavage of PIP_2 into DAG and IP_3. Figure adapted from Janeway's Immunobiology by Murphy [24].

1.3. Clusters of Proteins

In the past, many papers stated that the plasma membrane of cells is highly compartmentalized [4]. One of the first theories in this respect was the 'lipid raft model' stated by Simons and van der Meer in 1988. This theory states that specific regions of the cell plasma membrane are enriched by sphingolipids and cholesterol. It was assumed that lipid rafts can act as platforms where proteins can attach and interact with each other. Therefore, rafts could be also essential for signal transduction inside a cell [26]. There is a high amount of controversy about the existence, size and lifetime of such lipid rafts. Nowadays, the existence of large and long-lasting lipid rafts is seen as an exception [4].

A finding of plasma membrane compartmentalization in T cells was the discovery of specific protein rearrangement within the the immunological synapse (IS), which is the interface of a T

cell and an APC. Upon T cell activation the TCR forms so-called microclusters, which recruit other important signaling proteins. Eventually, T cell activation leads to an accumulation of the TCR in the center of the IS. The accumulation of TCR in the center of the IS is called central supra-molecular activation cluster (c-SMAC). Also, molecules as CD4 or CD8 are located in the c-SMAC. Proteins which are important for cell-cell adhesion, like LFA-1, accumulate around this c-SMAC in an area which is called peripheral SMAC (p-SMAC). It was found that early events of T cell activation, like phosphorylation of CD3 chains, Lck and ZAP-70 already occur previously to the formation of c-SMAC within microcluster [27].

After the development of superresolution microscopy methods, like (d)STORM, a lot of results suggesting the existence of protein nanoclusters were published. These results indicated that nearly all membrane proteins in mammalian cells form cluster at the nanometer scale [4]. Also T cells were investigated and nanocluster existence was evaluated for different proteins involved in the immunological response [4]. Experiments done by different groups found the TCR in nanoclusters, even in the resting state [28][29]. Kumar et al. found a different ratio of TCR nanocluster in naïve and memory T cells and therefore stated that T cells can regulate the amount of nanoclusters to act in different ways, like to facilitate a quick response [30]. Pageon et al. used dSTORM to evaluate the influence of TCR nanoclusters on signaling after activation. They published results suggesting that the density of TCRs in nanoclusters correlates with the signaling efficiency. According to their data the probability of phosphorylation of an individual TCR-CD3 complex depends strongly on the distance to the next TCR-CD3 complexes, and therefore on the density within a nanocluster. They proposed that the cluster density can change after pMHC binding, which means antigen recognition is converted into a density signal. Then the density is converted into a biochemical signal, i.e. the amount of phosphorylated CD3 complexes [31]. In addition to the TCR also other proteins involved in T cell activation were investigated. Roh et al. investigated for example CD4 and found nanoclusters containing CD4, which did not colocalize with TCR nanoclusters. The only interaction of TCR nanoclusters and CD4 nanocluster was found upon activation at the boundaries of both cluster types [32]. Reported nanocluster of TCR are between 30 nm – 300 nm in diameter [33]. Suggested reasons for the advantage of nanoclusters over randomly distributed proteins are for example the increase of ligand-binding affinity and the dwell time of ligands due to rebinding [4].

However, in recent studies inconsistencies were published which appear due to imaging artefacts when using superresolution microscopy methods like PALM and (d)STORM. These can influence results and lead to the observation of nanoclusters even if such compartments do

not exist [5] [34] [35]. One artefact leading to spurious results in respect to nanoclusters is the multiple observation of one single blinking fluorophore (overcounting) and missing observations because molecules are not labeled or fluorophore inactivity and bleaching (undercounting) [34] [33] [36].

1.3.1. Artefact free cluster analysis of membrane proteins

Since the identification of imaging artefacts in single molecule localization microscopy (SMLM), research groups try to compensate for them. Annibale et al. tried to get rid of temporal clustering assuming that this leads to multiple observations of the exact same fluorophore in a short period of time. They then combined all localizations within a certain radius and within a certain time [34]. On the other hand, Baumgart et al. developed an experimental method combined with an analysis routine to evaluate nanoclusters of proteins without sensitivity to the blinking statistics of the used fluorophores. The approach uses different image characteristics under conditions where the label density is varied. For various label densities, the following parameters are calculated during the analysis: the number of total localizations per μm^2, the relative area coverage by clusters (η) and the average density of localizations within the apparent clusters (ρ). Analyzing the area of clusters η and the density ρ in dependence of the localizations per μm^2 showed a difference between randomly distributed and clustered molecules for simulated data. For randomly distributed molecules, the area η increases steadily with the increasing labeling density, but the density of localizations per cluster remains constant. In case of clustered molecules, the relative area of clusters saturates, but the density is increasing linearly with increasing labeling density. These effects can be seen in **Figure 13**. The intersection of ρ and the y-axis is called ρ_0 i.e. the normalized localization density within clusters. By plotting ρ/ρ_0 versus η a clear difference between randomly distributed molecules and clustered ones is observed. This plot shows a steady increase for clustered molecules, but a more constant course for randomly distributed molecules [36]. By using this technique, Rossboth et al. could not confirm the existence of TCR nanocluster in non-activated mouse T-cells [33].

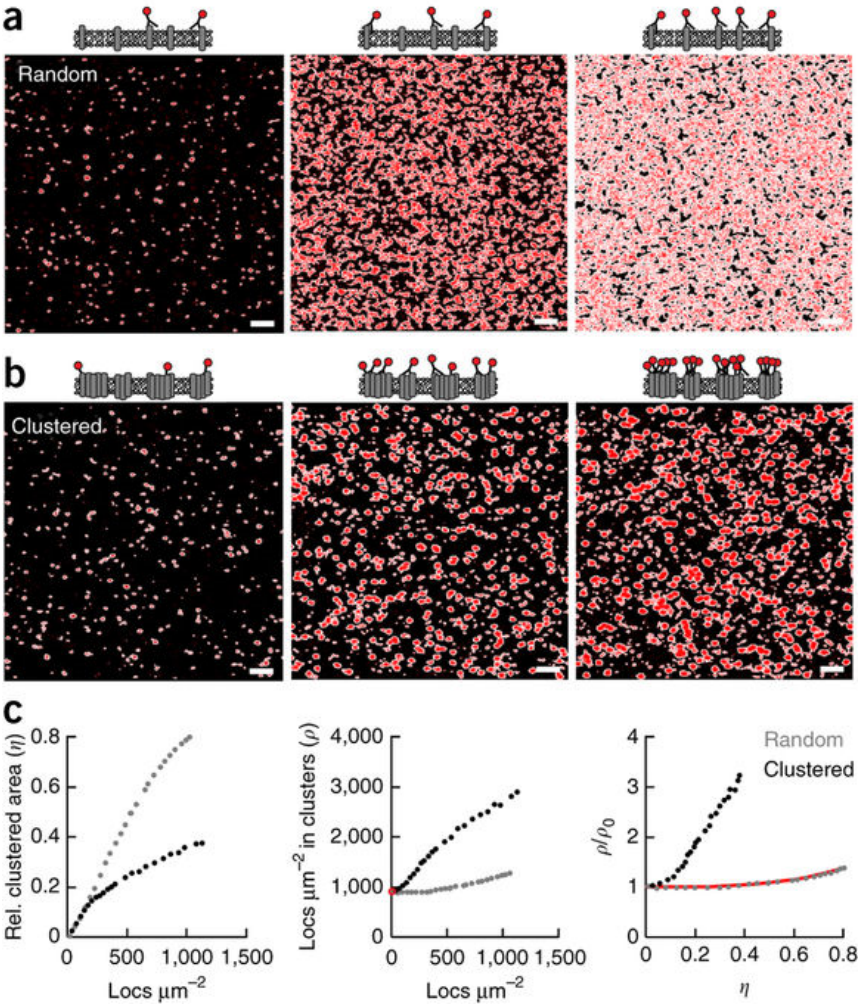

Figure 13: Label density variation for cluster detection. a) shows simulated data of randomly distributed molecules with different labeling densities and b) the same data, but for clustered molecules. Total localizations per µm², the relative area of analyzed clusters (η) and the density of these clusters (ρ) is calculated. Increasing the labeling density leads to an increase of the total localizations per µm² and to a steady increase of the relative area for randomly distributed molecules, whereas the curve of the clustered one saturates. The density of the clusters increases steadily for clustered molecules but is almost constant for random ones. Plotting a normalized density vs. the area of clusters results in a characteristic difference between random molecules and clustered ones. Figure adapted from Baumgart et al. [36].

The method used in the present thesis was suggested by Magdalena Schneider and uses two-color single-molecule microscopy [7]. The principle of this method is to use two different fluorophores to label the same protein of interest. If a molecule is located in a cluster, both colors can be detected within a small region. On the other hand side, if blinking of the fluorophore leads to many localizations in a small region (cluster), only a single color will be detected during the measurement. This principle can be seen in **Figure 14**.

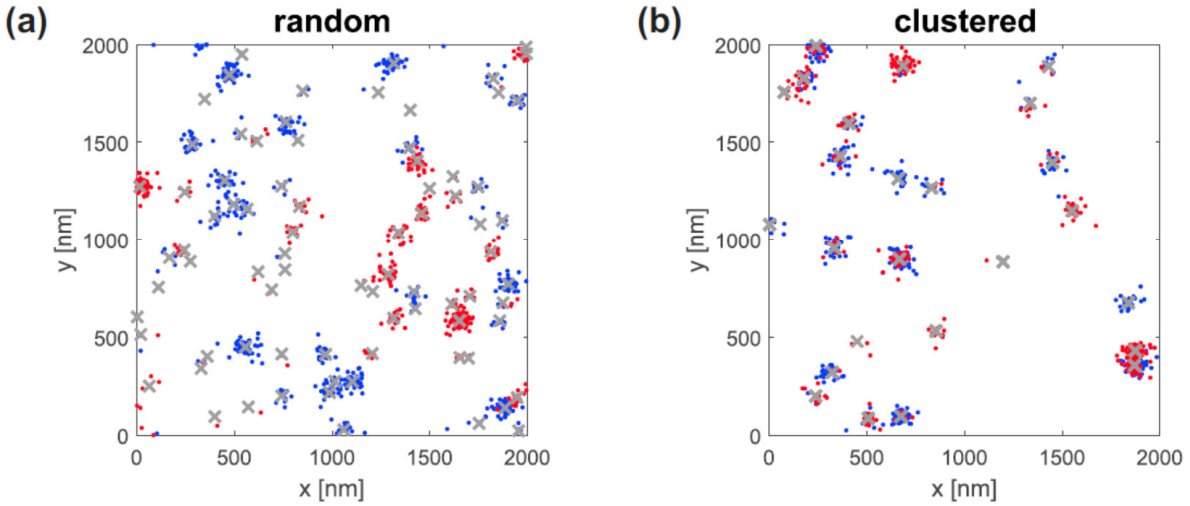

Figure 14: Difference for randomly distributed molecules and clustered ones in a two-color measurement. a) If the molecules are randomly distributed, localizations which seem to come from a cluster will be of only one color. On the other hand, if there are clustered molecules, these can be labeled by both colors and one will detect two different color signals in a small region. Figure adapted from Magdalena Schneider [7].

For this new method, each localization is taken and the distance to the nearest neighbor in the second color channel is calculated. To get randomly distributed data used as null hypothesis, toroidal shifts are applied to one of the color channels. Due to this any correlation between the two colors can be dissolved. By comparing the distribution of nearest neighbor distances of the original image and the distribution created by toroidal shifts real cluster can be detected, without detecting clusters due to fluorophore blinking. The method is described in more detail in chapter 2.6 [7].

1.4. Spatial distribution of the ER during T cell activation

In addition to the spatial distribution of the TCR, also the spatial organization of the endoplasmic reticulum during T cell activation was investigated in this thesis. The ER is an internal cell structure which consists of tubules and flattened sacs which are connected to a netlike structure and expands throughout the complete cytosol. The cavity created by this netlike structure is called ER lumen, which is enclosed by the ER membrane. There are two versions of the ER, the rough ER where ribosomes can bind for protein biosynthesis and the smooth ER. Besides its tasks of protein and lipid biosynthesis it acts as intracellular Ca^{2+} storage which is crucial in case of cell signaling, like during T cell activation [37] [38]. The

process of the ER binding to the cell plasma membrane after depletion of the internal Ca^{2+} storage was already mentioned previously and illustrated in **Figure 15**.

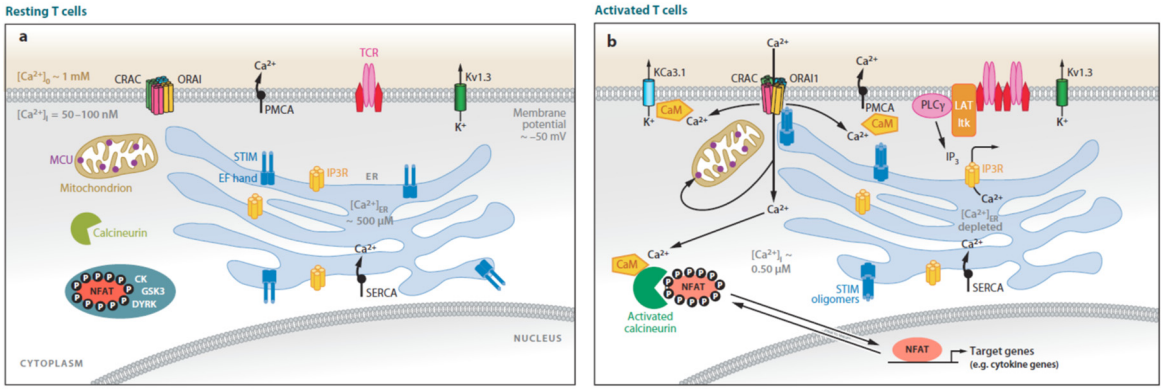

Figure 15: Pathway of Ca^{2+} signalling in T cells upon activation. Due to activation of the T cell IP_3 diffuses to the ER membrane and binds to IP_3 receptors which act as Ca^{2+} channels. Therefore Ca^{2+} flows from the ER lumen into the cytosol. After depletion of Ca^{2+} in the ER the sensor protein STIM1 oligomerizes and binds to ORAI located in the plasma membrane. This leads to the opening of CRAC channels and allows an influx of Ca^{2+} from outside the cell. Finally, the transcription factor NFAT is activated. Figure adapted from Hogan et al. [25].

2. Material and Methods

2.1. Cell culture

For all experiments, primary mouse cells were used and cultured in RPMI 1640 medium (Sigma-Aldrich) supplemented with 10% FBS (fetal bovine serum, Sigma-Aldrich), 1 kU/ml penicillin-streptomycin (Sigma-Aldrich), 2 mM L-glutamine (Sigma-Aldrich), 1 mM sodium pyruvate and 50 µM β-mercaptoethanol (Sigma-Adrich). Cells were isolated at the Medical University of Vienna as described previously by Huppa et al. [39]. Briefly, T cells were isolated fromthe spleen from 5c.c7 mice. These cells were cultured 7-9 days in the presence of 1 µM moth cytochrome c (mcc) peptide. After 24 hours, IL-2 was added. Before each experiment (6 days after isolation), viable and dead cells were separated using Histopaque 1119 (Sigma-Aldrich) and centrifugation. This separated dead from live cells based on different densities. Cells were grown at 37 °C and 5% CO_2 in humidified atmosphere.

2.2. Preparation of glass-supported lipid bilayers

For all experiments, glass-supported lipid bilayers (SLBs) were prepared. To this end, small lipid vesicles are spread on a hydrophilic surface. It is possible to generate SLBs from different mixtures of lipids, creating a two-dimensional system which allows the free diffusion of lipids and proteins anchored to lipids in the bilayer system. This potential diffusion makes SLBs a prominent tool to study compartmentalization of membranes [40]. To make a SLB functional, proteins are linked to the lipids. There are different methods for this process, the one used in this work uses lipid molecules with nitrilotriacetic acid in the head group (NTA). Proteins containing histidine tags bind to these NTA lipids with Ni^{2+} ions [41].

Lipids used were from Avanti Polar Lipids and a vesicle mixture composed of 90% 1-palmitoyl-2oleoyl-sn-glycerol-3-phosphocholine (POPC) and 10% 1,2-dioleoyl-sn-glycero-3-[(N-(5-amino-1-carboxypentyl)iminodiacetic acid)succinyl] (Ni^{2+}-DOGS) was used. Eight-well LabTek chambers were used for microscopy. These were prepared by removing the original slide on the bottom of the chamber and gluing a glass cover slide from Menzel (24 mm x 60 mmm #1.5) onto the bottom of the chamber. To achieve a hydrophilic surface needed for bilayer spreading, the prepared chamber was plasma cleaned for 10 min. 150 µl of POPC/10% Ni^{2+}-DOGS lipid mixture diluted in 1x PBS were pipetted into each well of the LabTek chamber. Chambers were incubated with the lipid mixture for 15 min at room temperature.

Then, every well of the chamber was rinsed with 25 ml PBS. In all experiments, activated and non-activated T cells were compared. Wells for non-activated T cells and wells for activated T cells differed by the attached proteins. His10-ICAM-1 from Sino Biologicals was used for non-activated wells to guarantee attachment of the T cells without activation. Wells for activated T cells were prepared with His10-ICAM-1 for adhesion, with mcc-His12-I-E^k for activation and His10-B7-1 (Sino Biologicals) to achieve co-stimulation through CD28. After 90 min incubation at room temperature the wells were rinsed again with PBS. Before seeding the cells, PBS was exchanged with Hanks' Balanced Salt solution (HBSS; Lonza) by five times sequential dilution of 500 ml portions.

2.3. Labeling of T cells for two-color cluster analysis

As mentioned in chapter 1.3.1, the analysis method depends on labeling one protein with two different fluorophores. About 10^6 cells were washed with HBSS and unspecific binding sites were blocked using 5% BSA (Sigma-Aldrich) diluted in HBSS for 10 min on ice. Afterwards, cells were labeled for 20 min on ice with 10 µg/ml of Alexa Fluor 647 anti-mouse TCR β chain specific antibody (clone H57-597, catalog number 109218, Lot: B206104, BioLegend) (last experiment: catalog number 109217, Lot: B241822) (H57-AF647) [42] and 10 µg/ml Alexa Fluor 488 anti-mouse TCR β chain specific antibody (clone H57-597, catalog number: 109215, Lot: B195696, BioLegend) (H57-AF488) [43], both diluted in 5% BSA/HBSS. After labeling, cells were washed two times with HBSS. Cells were resuspended in 20 µl HBSS/well and seeded into the prepared. 10^6 cells were used for a total of four wells. Incubation was conducted at 37 °C for 3 min (two wells, one activating and one non-activating), or for 5 min (two remaining wells, one activating and one non-activating). After this incubation step, cells were fixed with a final concentration of 4% PFA + 0,2% GA diluted in PBS for 30 min. Afterwards PFA was exchanged with HBSS by 5 times sequential dilution of 500 µl portions.

For two-color dSTORM measurements Oxea buffer was used [20]. The buffer consists of 50 mM β-mercapto-ethylamine hydrochloride, 3% (v/v) OxyFlour and 20% (v/v) sodium DL-lactate solution in PBS. The pH was adjusted to 8-8,5 with NaOH. HBSS in wells was exchanged with this buffer by two times sequential dilution of 500 µl portions shortly before measurement.

2.4. Labeling of T cells for TCR vs. ER measurements

In this experiment two structures of T cells were observed simultaneously, the TCR and the ER. About 10^6 primary T cells were taken and washed with HBSS. The labeling of the endoplasmic reticulum was realized by using the Cytopainter staining kit form Abcam [44]. First, the 10x Assay Buffer contained in the Cytopainter kit wad diluted with deionized water to obtain 6 ml of 1x buffer. Next, the detection agent within the Cytopainter set was diluted 1:5000 in 1x assay buffer. 1 ml of the diluted detection agent was used to label cells for 20 min at 37 °C. Afterwards, cells were washed two times using 1 ml of 1x assay buffer. After washing, unspecific binding sites were blocked using 5% BSA for 10 min on ice. After blocking, cells were labeled with 10 µg/ml of Alexa Fluor 647 anti-mouse TCR β chain specific antibody (clone H57-597, catalog number 109218, Lot: B206104, BioLegend) [42] diluted in 5% BSA/HBSS. Labeling lasted for 20 min on ice. Next, cells were washed two times with HBSS and resuspended in HBSS. Then 20 µl of cell suspension was seeded in every well of a LabTek chamber prepared with a SLB. In the experiments, activating and non-activating conditions and different incubation times were compared. Incubation lasted depending on the experiment between 2 min and 15 min for activating and non-activating conditions. After the incubation at 37°C, cells were fixed at a final concentration of 4% PFA and 0,2% GA diluted in PBS. After 10 min of fixation, PFA was exchanged with HBSS by five times sequential dilution of 500 µl portions

2.5. Microscope setup

Imaging was conducted on a Zeiss Axiovert 200 microscope with a 100x Zeiss Apochromat oil immersion objective with a numerical aperture of 1,46. For two-color dSTORM measurements a 640 nm diode laser (Coherent OBIS LX FP 75 mW), a 488 nm diode laser (Toptica iBeam smart 200 mW) and a 405 nm UV laser (Coherent Innova 90C) were used. For diffraction limited imaging in case of TCR vs ER measurements only the 640 nm diode laser in combination with the 488 nm diode laser were used. To modulate the intensity of the lasers for imaging and focusing, acousto-optic modulators (AOMs) were used. The 640 nm laser and the 488 nm laser were combined with an OBIS galaxy laser beam combiner and after decoupling from the fiber, overlaid with the 405 nm laser by a dichroic mirror. A telescope was used to focus the laser beams into the back focal plane of the objective. Coupling of the laser beams into the microscope was realized with a periscope. One of the periscope mirrors was

placed on a moveable stage which allows shifting of the laser beams parallel to the optical axis. By this, TIRF imaging is realized. The emitted light coming from the sample was split by its color with a dichroic mirror (Cairn Research Optosplit) and therefore projected onto two different regions on the camera chip simultaneously. The described setup is schematically illustrated in **Figure 16**.

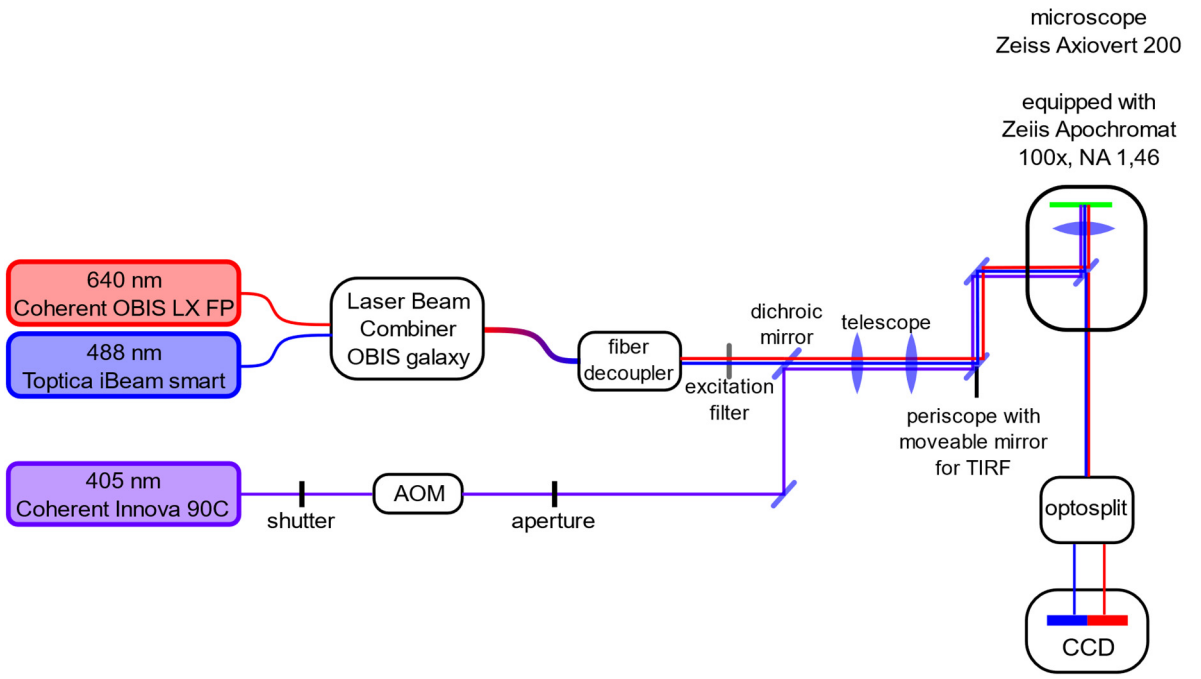

Figure 16: Schematic overview of the used microscopy setup. For measurements, three different laser lines were used (640 nm, 488 nm and 405 nm). After combination of all laser lines with a dichroic mirror, the beams were coupled into the microscope by using a periscope with a movable mirror. This mirror is used to realize TIRF by shifting the beams parallel to the optical axis. The emitted light from the sample is split depending on their color (their responsible emitter-fluorophores) into two parts which are guided to different places on the camera chip. The shown telescope is needed to focus the laser beams into the back focal plane of the objective.

2.5.1. Two-color image registration

Before recording a two-color experiment, images of a bead sample were taken and later used for color correction. The bead sample was illuminated by the 640 nm and 488 nm laser and the dichroic mirror, which splits the emitted light from the red and the blue laser, was adjusted. After adjustment, the channel of 640 nm excitation illuminated the left half of the camera chip, and the channel of 488 nm excitation illuminated the right half of the camera chip. Two images of the same beads were taken, first an image by illuminating with the red laser, the second image by illumination with the blue laser. During analysis, the position of a bead in the red channel and its position in the blue channel is measured. By determining the position deviation between the red and the blue channel of about 60 different beads, which should be distributed

over the whole region of interest, it is possible to calculate parameters for shifting and stretching the x and y axis of one channel to generate an exact overlay of both. This shift- and stretch-transformation can be used later to correct the dSTORM data.

2.5.2. Two-color dSTORM

For imaging, an already existing in-house developed LabView software was used. The illumination protocol used is shown in **Figure 17**. The protocol depicts how long which laser illuminated the sample and at which times the camera chip was illuminated and read out. The illumination cycle starts by illumination of the sample with the 640 nm laser for a specified illumination time t_{ill}. In two-color dSTORM experiments t_{ill} was set to 1 ms. Simultaneously, the camera chip was illuminated for the same time and read out. The read-out time of the camera was used to illuminate the sample with the UV laser (405 nm) to facilitate blinking of the fluorophores. UV laser illumination lasted for 6 ms. After 6 ms the sample was illuminated with the blue laser (488 nm) for 1 ms. This illumination cycle was repeated 12000 times, leading to a total frame number of 24000.

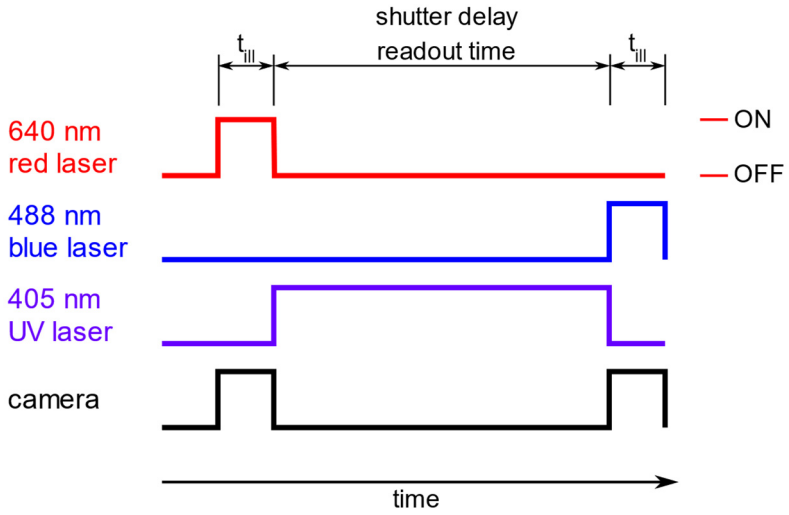

Figure 17: Illumination protocol for two-color dSTORM measurements, in this case with the 640 nm and the 488 nm laser. Blinking of the fluorophore was achieved by illumination with the 405 nm UV laser. The illumination time in the presented experiments was 1 ms, shutter delay was set to 6 ms. During the illumination of the sample with either the red or the blue laser, the camera was exposed as well.

2.5.3. Imaging of two-color TCR vs. ER

All images were recorded with the already mentioned in-house developed LabView software. The TCR was labeled with H57-AF647. The Cytopainter from Abcam which binds to the endoplasmic reticulum gets excited by the blue laser. Therefore, these two laser lines were used

for imaging. After tuning of the Optosplit cube and imaging the bead samples, diffraction limited images were recorded in TIRF mode. For every cell, one image was recorded by illumination with the red laser. This image contained signals from the TCR. The second image was recorded from the same cell by illuminating it with the blue laser to image the ER. In both cases the illumination time was set to 3 ms.

2.6. Analysis of two-color dSTORM experiments

After measurement, the image stack was divided in two stacks, one including the measured signals during illumination with the 640 nm laser, the other one including the measured signals during illumination with the 488 nm laser. Both stacks consisted of 12000 frames. Fiji [45] and the plugin ThunderSTORM [46] were used for single-molecule signal localization within all image stacks. Following camera settings were used: pixel size 100 nm, photoelectrons per A/D count 16.4, base level 100 and EM gain 300. ThunderSTORM allows for many different settings for the emitter localization fitting. First, the images are filtered. **Table 1** shows the parameters of the used Wavlet filter which acts as bandpass to reduce noise.

Table 1: Parameters used for filtering the recorded datasets before fitting of the emitter positions

Image filtering	
Filter Type	Wavelet filter (B-Spline)
B-Spline Scale	2
B-Spline Order	3

After filtering, approximate emitter positions were detected by comparing pixel values with a given threshold. This threshold was varied within experiments. Data were evaluated with fixed thresholds (75, 100, 150) and thresholds depending on the standard deviation of the first wavelet level multiplied by a constant. This constant was set to values of 1, 1.5 and 2.5 (see **Table 2**). Later it was decided which threshold would led to the best result by considering the ability to detect emitters and do not detect signals coming from background and noise.

Table 2: Parameters used for approximate localization of molecules in ThunderSTORM

Approximate localization of molecules	
Method	Local maximum
Pixel Intensity Threshold	Varying: fix or constant*std(Wave.F1)
Connectivity	8 neighborhood

After the approximate localization, pixels with signals from a detected emitter remain. To obtain the exact position of the emitter, the values of these pixels are fitted using a Gaussian function to approximate the point spread function (PSF). The parameters are shown in **Table 3**. This analysis results in a table with x and y positions of the fitted emitters.

Table 3: Fitting parameters used in ThunderSTORM to obtain the exact emitter positions

Sub-pixel localization of molecules	
Method	PSF: Integrated Gaussian
Fitradius	3
Method	Least squares

Following filters were used to postprocess the loclaizations after the fitting procedure:

- median(intensity)-std(intensity) < intensity < median(intensity)+std(intensity)
- median(uncertainty)-1.5*std(uncertainty) < uncertainty < median(uncertainty)+1.5*std(uncertainty)
- 0.6*median(sigma) < sigma < 1.4*median(sigma)

2.6.1. Cluster analysis

As already mentioned in chapter 1.3.1, a method described by Magdalena Schneider was used for cluster analysis. In the following chapter, the single steps and the background of this method are described in more detail. Using ThunderSTORM results in tables with the positions of the fitted emitters. These can be represented in a localization map. Such a result-table is available for the red as well as for the blue color channel. By using the transformation parameters acquired by the method described in chapter 2.5.1, the positions of the blue color channel are corrected for chromatic aberrations and shifts. For cluster detection, each target molecule is labeled with two different fluorophores. In the case of real molecular clustering, each molecule in the cluster can be labeled by fluorophores of different colors. If molecules are randomly distributed and a localization cluster is due to fluorophore blinking, the localization cluster will be composed of only one of the two colors. As a consequence, clustered molecules tend to have a smaller nearest-neighbor-distance to localizations in the second color channel compared to molecules which are randomly distributed. To measure this difference and to decide whether a molecule is randomly distributed or clustered, the cumulative distribution of nearest-neighbor-distances is used. In addition, we wanted to evaluate the results by applying a statistical test.

This requires the formulation of a null hypothesis (H_0). In our case, the null H_0 is the cumulative nearest-neighbor-distribution of randomly distributed molecules. Since, there is no general H_0 to which data from every cell could be compared. we used toroidal shift randomization [47] to generate randomized data from each measurement. To this end, the localizations from one channel are shifted by a random vector in x and y direction, while the localization within the second channel remain on their original position. The mathematical representation of this method is shown in **Formula 8**. By this technique it is possible to break up dependencies of the two different color channels which appear if the molecule is located in a real cluster.

$$(x_{new}, y_{new}) = (x, y) + (x_{shift}, y_{shift}) \qquad (8)$$

The values for the toroidal shift were picked from a uniform distribution in fixed intervals. The maximal shift values were given by the size of the region of interest which was picked for analysis. The minimal value for the shift was set to 100 nm to assure shifts with a minimal distance of the reported size of a nanocluster. The toroidal shift is illustrated in **Figure 18**. The figure shows that due to the shifting process, localizations of some areas would lie outside of the observation region. To avoid this, the pattern is reassembled according to **Figure 18b**. The lower row of **Figure 18** shows how this toroidal shift looks for simulated data which show clustering of molecules. Due to the shifting process, the dependencies between the blue and the red channel are dissolved. To get a more reliable result when conducting the statistical test, the original data is not only compared with data after one toroidal shift, but it is compared with data of 99 different shifts. The more randomized data sets are generated, the higher is the reliability of the results. However, too many control models would lead to an excessive computational time.

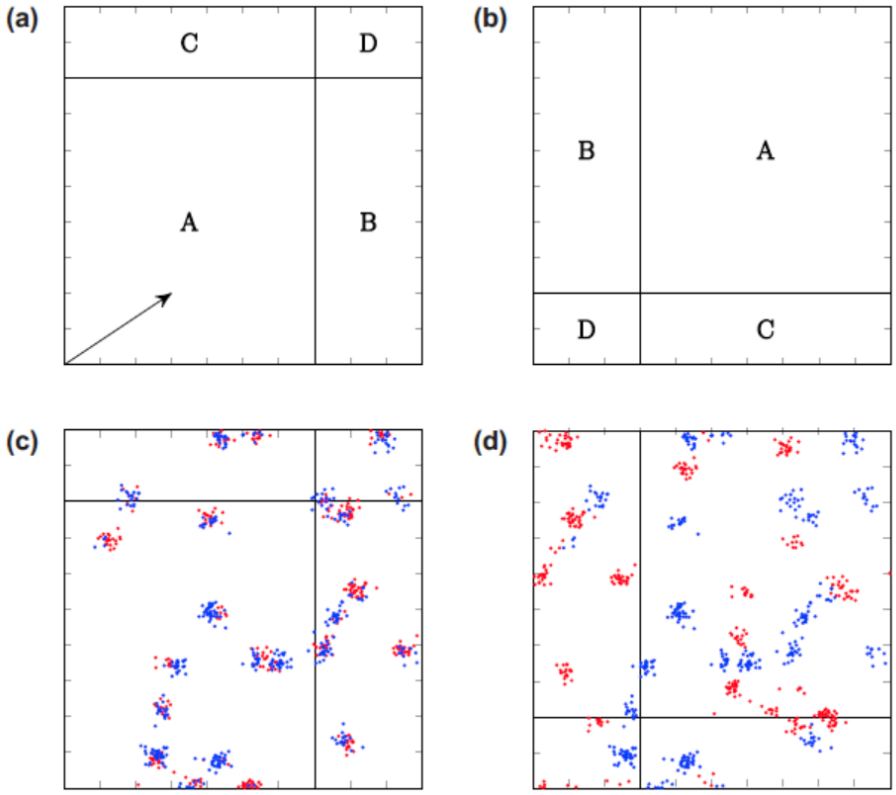

Figure 18: Toroidal shift. The localizations of one channel are shifted by a random shift vector, shown in a. This would lead to the effect, that localizations of the areas C, D and B would lie outside of the observation region. Therefore, the regions are assembled in a new manner, illustrated in panel b. Panels c and d show how this model breaks the correlation of the two-color channels in case of clustered molecules. Figure is adapted from Magdalena Schneider [7].

After generation of all 99 shifted models, the distance of every localization of channel 1 to its nearest neighbor in the second channel was calculated. This calculation was done for the original data and all 99 shifted models. Afterwards, the cumulative distribution function of the nearest-neighbor-distances was calculated by **Formula 9**. The cumulative distribution function of the nearest-neighbor-distances gives the probability if the nearest-neighbor-distance is less than or equal to a certain value d.

$$F_D(d) = \mathbb{P}(D \leq d) = \int_0^d f(r)dr \qquad (9)$$

Here *f(r)* represents the probability distribution function of the nearest-neighbor-distances. For the statistical test, the cumulative distributions functions of all 99 controls are averaged by **Formula 10**, where n is the number of control models (99 in our case) and $F_i(x)$ the cumulative distance distribution of a certain control model i. This averaged function *F(x)* is used as null

hypothesis for randomly distributed molecules. Typical CDF functions are illustrated in **Figure 19**

$$F(x) = \frac{1}{n}\sum_{i=1}^{n} F_i(x) \qquad (10)$$

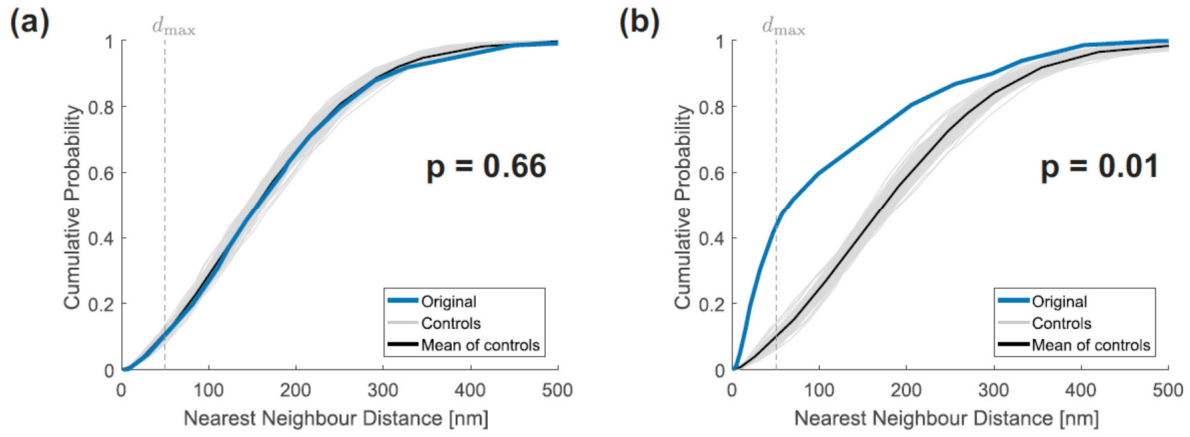

Figure 19: Cumulative distribution functions of nearest-neighbour-distances. In both cases the blue line illustrates the CDF of the original localizations. The gray lines are CDFs calculated from the 99 control models and the black line is the average CDF of all control models. Panel a shows a typical CDF of a randomly distributed dataset, whereas the blue CDF of panel b shows a high deviation compared to the mean CDF of the control models.

For comparison, the deviation of the fit between all cumulative nearest-neighbor-distributions (original and shifted ones) $F_i(x)$ and the mean cumulative distribution $F(x)$ was evaluated by **Formula 11**.

$$s_i = \int_0^{d_{max}} (F_i(x) - F(x))dx \qquad for\ i = 0\ to\ 99 \qquad (11)$$

Here, i is 0 for the cumulative distribution of the original data and 1 to 99 for cumulative distribution of the control models. The distance d_{max} determines in which area of the cumulative distribution function the fit of the curves is compared. In our case, the distance was set to 50 nm, which would include the detection of nanocluster. To calculate a p-value, **Formula 12** is used in which H is the so-called Heaviside step function and where si respectively s0 are the values calculated by **Formula 11**. The Heaviside step function is 0 if its argument is negative. When its argument is positive or equal to 0, the Heaviside step function is 1.

$$p = \frac{1}{n+1}\sum_{i=0}^{n} H(s_i - s_0) \qquad (12)$$

This calculation leads to small p-values if the s_0 value, obtained from the original data is higher than the s_i values obtained from the control models. This is the case, if the cumulative distribution of the original data shows a high deviation of the mean cumulative distribution of the control models (see **Formula 11**). This would for example be the case if molecules are located in cluster because then the cumulative distribution would be shifted to smaller nearest-neighbor-distances (high slope at the beginning). If the calculated p-value is below a certain level of significance, H_0 (a random distribution of molecules) is rejected and one can assume that the spatial distribution of the investigated molecule differs from the random distribution. In this thesis, the level of significance was set to 0.05 which is a commonly used value in statistics.

2.7. Analysis of two-color TCR vs. ER measurements

After measurement, two images with the size of 128 x 512 pixel for every cell were available. One image was recorded with illumination by the red laser, the second one by illumination with the blue laser. When using the red laser for illumination, the left half of the 128 x 512 pixel area was used for image recording. The right half got exposed upon illumination by the blue laser. In case of diffraction limited images of the cell, the mentioned method of color correction is not necessary. In case of diffraction limited images, it is enough to use the images taken from the bead sample to decide how the original 128 x 512 pixel images need to be cropped to obtain a red 128 x 128 and a blue 128 x 128 image which show a sufficiently accurate overlay. After cropping, the images were overlaid and also side by side images were created, to qualitatively judge if the position of the ER changes due to activation of the T cell and if there is a spatial reorganization upon T cell activation. To quantitatively judge the recruitment of the ER to the plasma membrane, the intensity of the blue channel was used. **Formula 13 to 15** describe the calculated parameter for a chosen region of interest (ROI) inside the cell with exclusion of membrane structures at the border of cells. **Formula 13** is the mean of all pixel values of the chosen ROI, **Formula 14** the standard deviation and **Formula 15** the so-called coefficient of variation. The coefficient of variation is defined as standard deviation divided by the mean and can be seen as a relative measure of variation. This fact makes it easy to compare also measurements which, for example, suffer from different mean intensities. This

can happen when data are recorded on different days and the background signal is different on both days.

In **Formula 13** the mean image intensity $\bar{I}$ is given, where n is the total number of pixels in the region of interest, and I_p the intensity value of a certain pixel p.

$$\bar{I} = \frac{1}{n}\sum_{p=1}^{n} I_p \qquad (13)$$

$$\sigma = \frac{1}{n-1}\sum_{p=1}^{n}\left(I_p - \bar{I}\right)^2 \qquad (14)$$

$$CV = \frac{\sigma}{\bar{I}} \qquad (15)$$

3. Results

Results of experiments investigating the spatial distribution of the TCR in non-activated and activated T cells are presented in chapter 3.1. Results describing the spatial distribution of the ER during T cell activation are presented in chapter 3.2.

3.1. Two-color dSTORM cluster analysis

The experiment investigating the spatial distribution of the TCR by using two-color dSTORM measurements was conducted seven times. However, for the first six experiments the results could not be properly analyzed, because there were too few localizations in the red channel. Localization maps of cells after ThunderSTORM analysis in **Figure 20** illustrate this problem. In **Figure 20a** there are only very few localizations in the red channel, in **Figure 20b**, the number of localizations inside and outside of the cell looks nearly identical. Further experiments were conducted to solve the problem, which arose from the fact that the fluorophore in the red channel did not show any blinking.

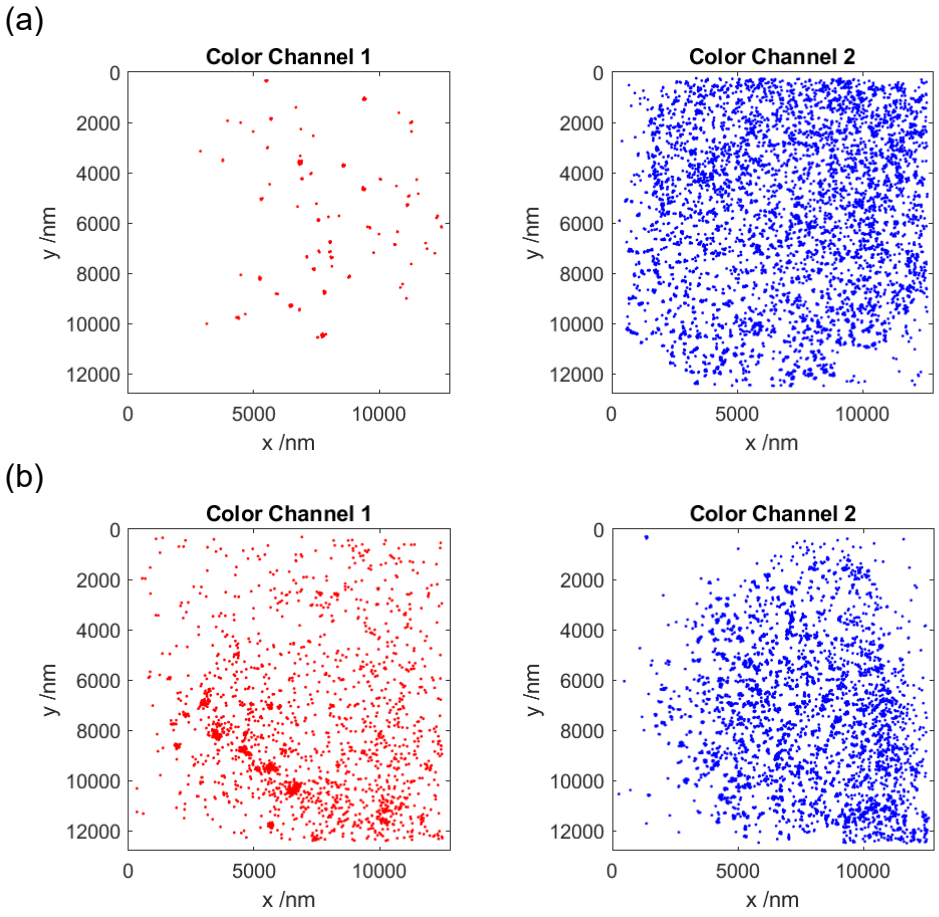

Figure 20: Exemplary localization maps of the first six experiments show only few localizations in the red channel (a) or nearly the same amount inside and outside of the cell shown in panel b.

Localization maps of representative cells of experiment 7 are shown in **Figure 21**. For these cells enough, localizations in both color channels can be seen. The original data showed sufficient blinking of both fluorophores. **Figure 21a** shows an example of the recorded 22 non-activated T cells, **Figure 21b** shows an example of the 14 recorded activated cells. The localization maps were created using ThunderSTORM. The first 2000 frames were excluded, because single molecule signals could only be reasonably detected after enough fluorophores were switched to a dark state by laser illumination.

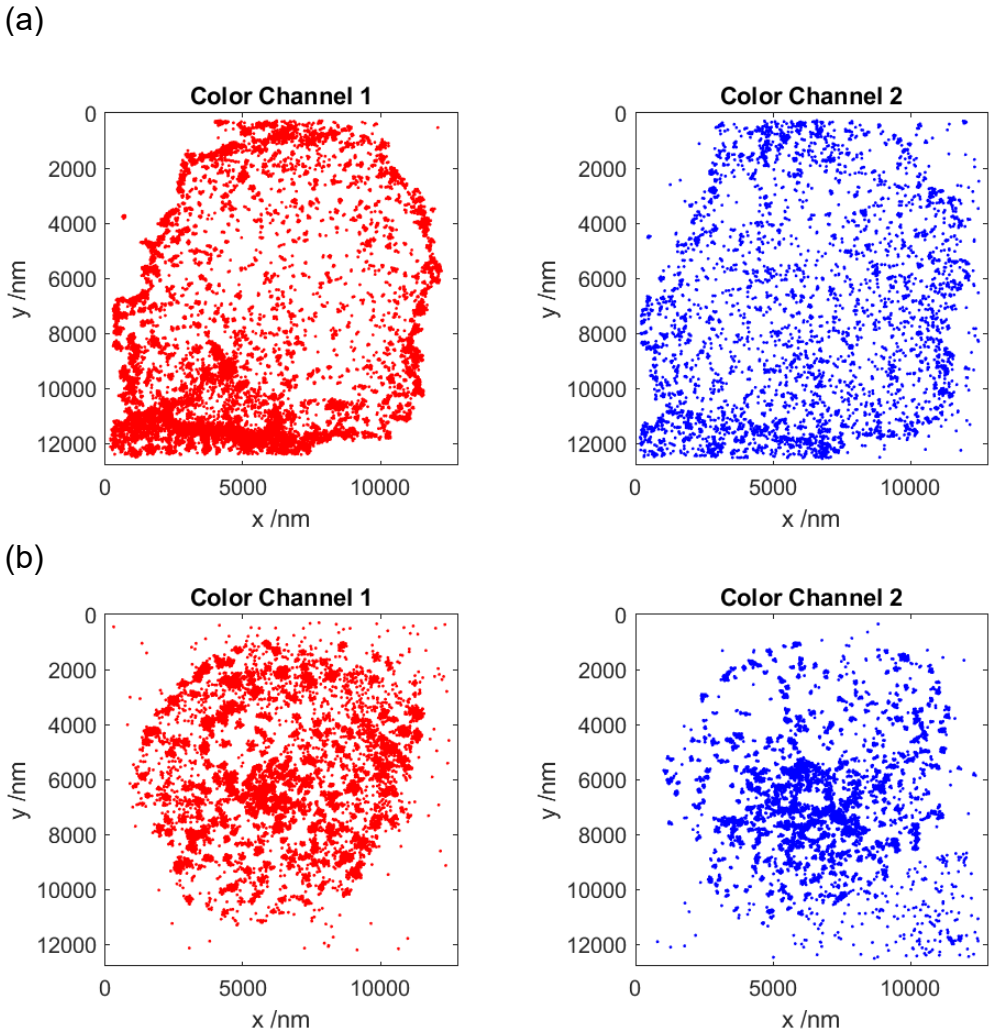

Figure 21: Exemplary localization maps of analyzed T cells of experiment 7. Panel a shows a non-activated cell, b shows an activated one. Left images represent localizations of TCRs labelled with H57-AF647, right ones represent localizations of TCRs labelled with H57-AF488. In both channels a sufficient amount of localizations is visible. The activated cell in the lower row shows microclusters and a c-SMAC.

After evaluating the p-values as described in chapter 2.6, p-values of non-activated and activated cells were illustrated in two separate histograms. For this experiment the analysis was conducted with different parameters. For the results in **Figure 22**, different intensity thresholds

for fitting in ThunderSTORM were used: specifically, we used 1.5*std (standard deviation) of the first level (F1) of the wavelet filter for filtering in the red channel and 2.5*std of F1 for the blue channel (for more detailed information regarding the used parameter see **Table 1** to **Table 3** in chapter 2.5.1). dSTORM measurements were conducted without a prior high-power illumination to transfer a majority of the fluorophores in a dark state. However, for the analysis, frames at the beginning, where emitter signals largely overlapped, were excluded. In case of the histogram in **Figure 22**, 2000 frames of the red and 2000 frames of the blue channel were excluded, leading to 10000 frames that were included in the analysis. The toroidal shift was applied to the blue channel. The distribution of p-values in **Figure 22** shows in both cases (non-activated cells **Figure 22a** and activated cells **Figure 22b** a distribution which is shifted to small p-values. However, the distribution of non-activated cells looks more uniform compared to the distribution for activated ones.

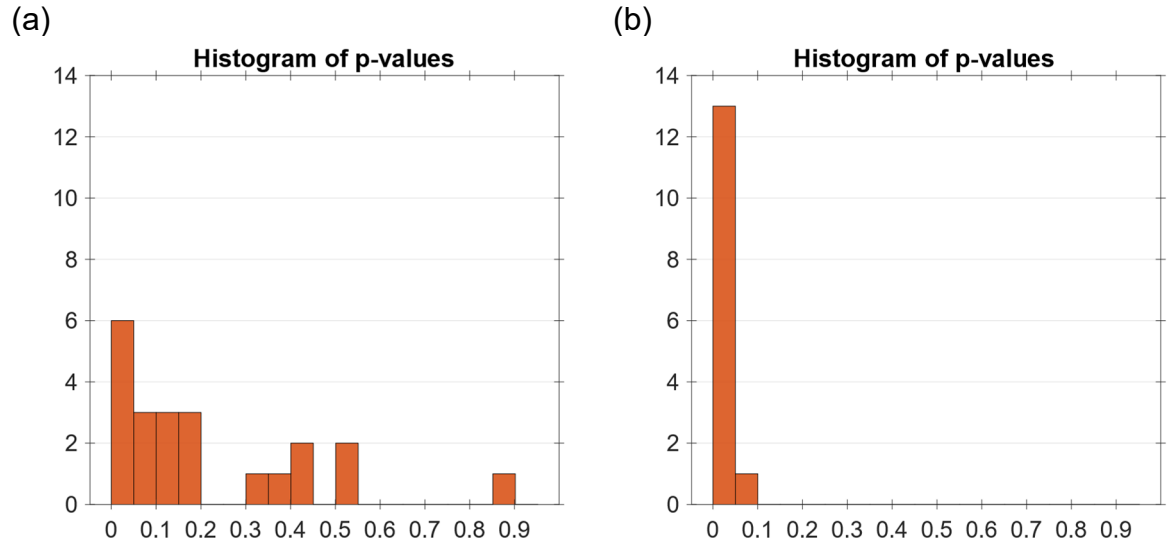

Figure 22: Evaluated p-values of non-activated (a) and activated (b) cells using intensity thresholds of 1.5*std of F1 of the used wavelet filter for the red channel and 2.5*std of F1 of the used wavelet filter for the blue channel. For both channels the first 2000 frames were excluded from analysis and the toroidal shift was applied to the blue channel.

p-values and the cumulative distribution of nearest neighbor distances of the exemplary cells shown in **Figure 21** are illustrated in **Figure 23**. **Figure 23a** shows the CDF for the non-activated, **Figure 23b** for the activated cell in **Figure 21**. In **Figure 23a** the CDF of the non-shifted data shows no deviation from the CDF generated from the localization maps after the toroidal shifts, which results in a p-value, which does not suggest a rejection of H_0. The CDF of the original data of the activated cell is characterized by a tendency to shorter nearest neighbor distances compared to the null models generated by the toroidal shift.

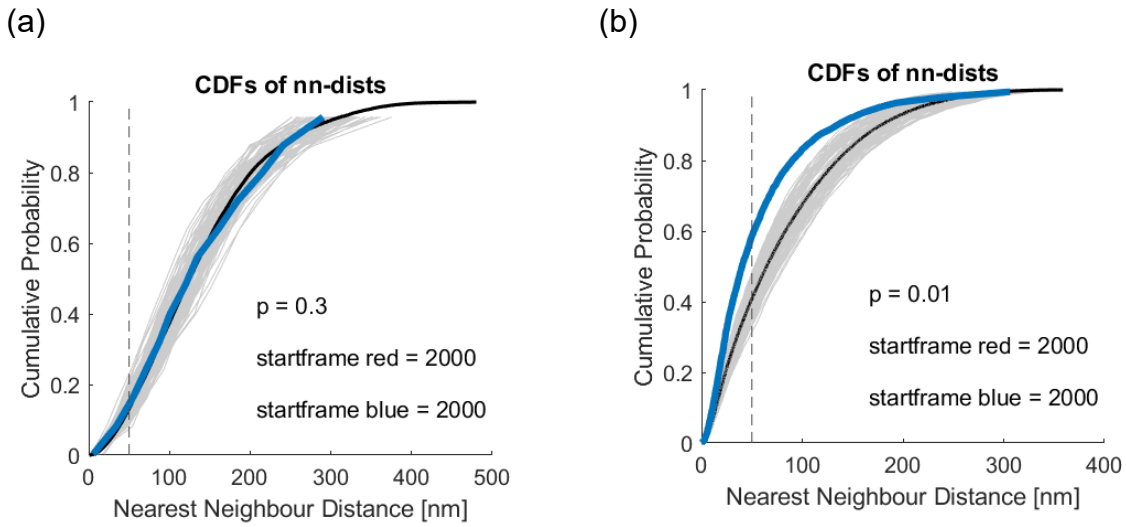

Figure 23: CDFs of nearest-neighbour distances of exemplary cells shown in **Figure 21**. Panel a depicts the CDF of the non-activated, panel b of the activated cell in **Figure 21**. The blue line is the CDF of the original localizations, the gray lines are CDFs of localizations after computing the toroidal shifts, and the black CDF illustrates the mean of all toroidal shift models. In a the blue CDF shows no deviation from the toroidal shift models, therefore, the p-value is above 0.05 which means that H_0 (randomly distributed emitters) cannot be rejected. In panel b the CDF of the data shows a strong deviation from the CDFs calculated from the toroidal shift data. This leads to a small p-value and rejection of H_0.

Plotting histograms of p-values calculated by using the same parameters as used for **Figure 22** but applying toroidal shifts to the red channel leads to results shown in **Figure 24**. The histograms show a slight difference to the ones generated by applying the toroidal shift to the blue channel.

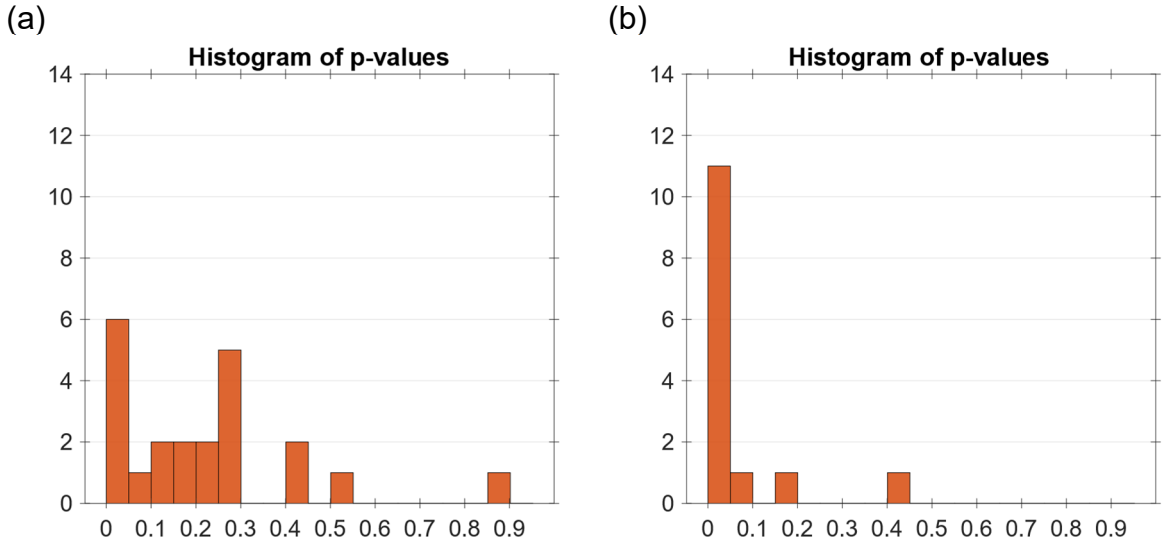

Figure 24: Evaluated p-values of non-activated (a) and activated (b) cells, using thresholds of 1.5*std of F1 of the used wavelet filter for the red channel and 2.5*std of F1 of the used wavelet filter for the blue channel. Further for both channels the first 2000 frames were excluded from analysis and toroidal shift model were generated for the red channel.

To evaluate the influence of the intensity threshold applied for single molecule localization using ThunderSTORM, the same analysis as in **Figure 22** and **Figure 24** was conducted with a threshold of 2.0*std of F1 of the used wavelet filter instead of 2.5*std for the blue channel. Every other threshold used during ThunderSTORM analysis lead to too few localizations (for example higher threshold as 1.5*std of F1 of the used wavelet filter in the red channel). On the other hand, using too low of a threshold, resulted in too many localizations due to fitting background noise (for example using lower thresholds than 2.0*std of F1 of the used wavelet filter for the blue channel). **Figure 25**, **Figure 25a** and **Figure 25b** show the results for calculating the toroidal shift models for the blue channel, **Figure 25c** and **Figure 25d** are the results for calculating the toroidal shift models for the red channel. Panels a and c show results for non-activated cells, panels b and d for activated ones.

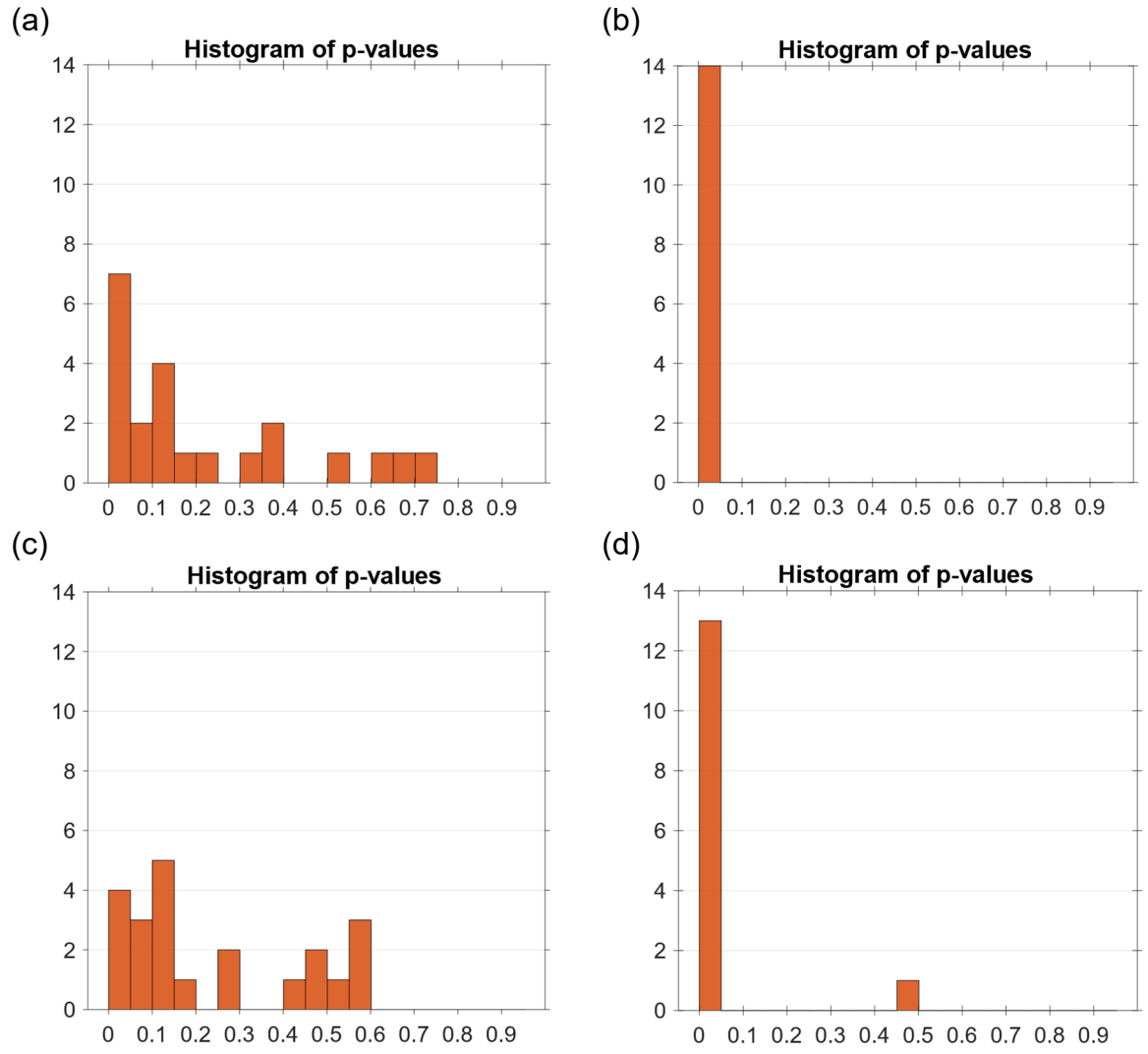

Figure 25: Evaluated p-values of non-activated (a and c) and activated (b and d) cells using thresholds of 1.5*std of F1 of the used wavelet filter for the red channel and 2.0*std of F1 of the used wavelet filter for the blue channel. For both channels the first 2000 frames were excluded from analysis. Panels a and b show results when toroidal shifts are calculated for the blue channel, c and d show results when the toroidal shift modes are calculated for the red channel.

Excluding 3000 frames at the beginning of the recorded movie instead of 2000 but leaving all other parameter as in **Figure 25** lead to p-value distribution shown in **Figure 26**.

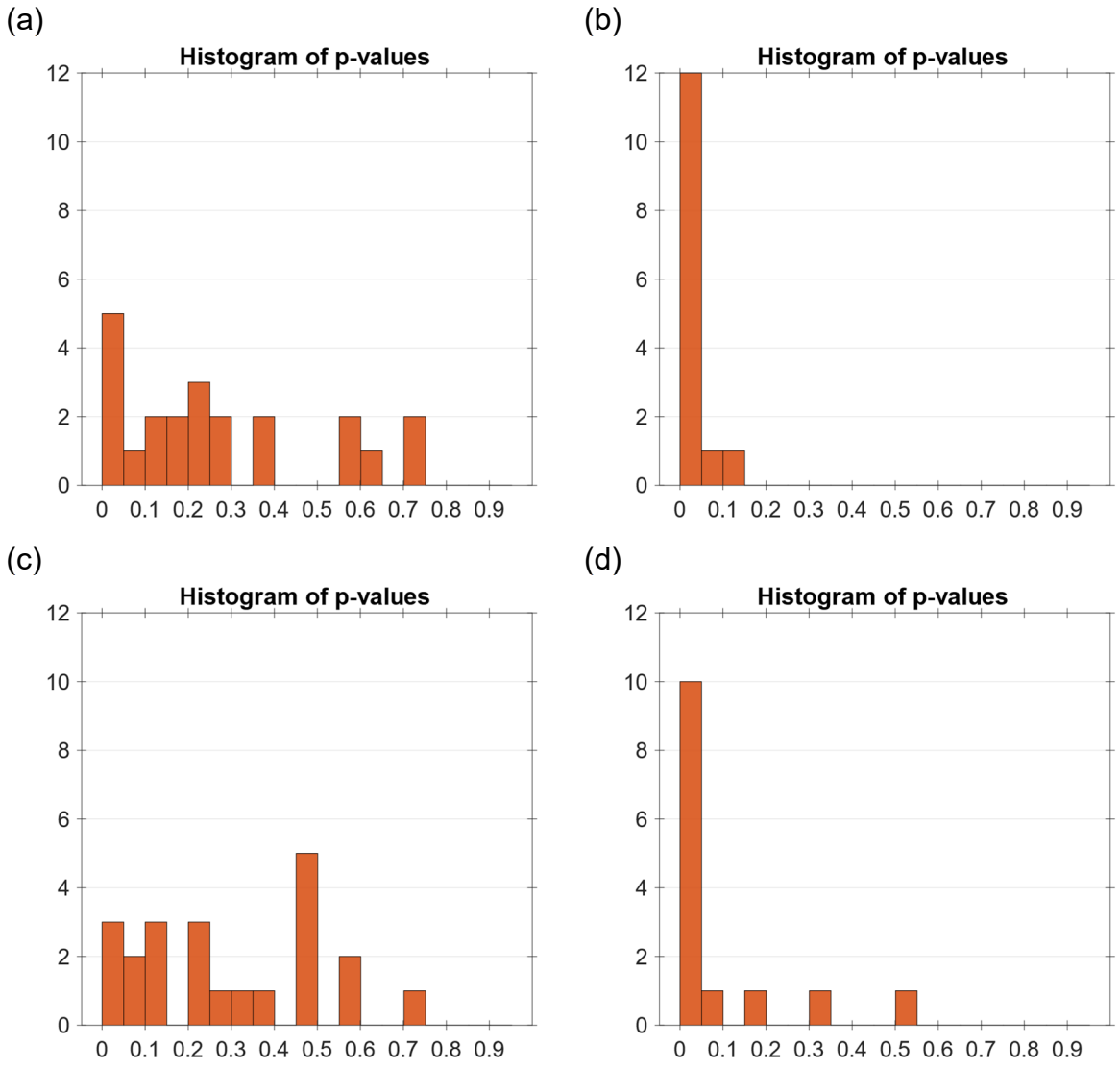

Figure 26: Evaluated p-values of non-activated (a and c) and activated (b and d) cells, using thresholds of 1.5*std of F1 of the used wavelet filter for the red channel and 2.0*std of F1 of the used wavelet filter for the blue channel. Further for both channels the first 3000 frames were excluded from analysis. Panels a and b show results when toroidal shifts are calculated for the blue channel, c and d show results when the toroidal shift modes are calculated for the red channel.

Figure 22, **Figure 24** but especially **Figure 25** and **Figure 26** show a clear difference between non-activated and activated cells. Looking at **Figure 25** and **Figure 26**, it can be clearly seen that more excluded frames at the beginning of the sequence lead to a more uniform distribution for non-activated cells. However, also p-values of some activated cells increase. Nevertheless, the distributions show a clear difference for non-activated and activated cells. Original data of

some non-activated cells with a p-values below 0.05 show in some cases strong background, like depicted in **Figure 27**.

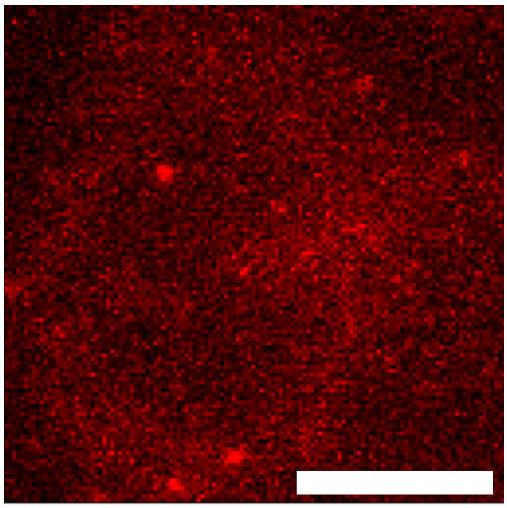

Figure 27: Original data recorded of a non-activated T cell. The image shows frame 2000 of the recorded movie. Beside some clear emitters, some cytosolic background can be clearly seen in the right half of the cell. Scale bar: 5 µm

3.2. Spatial distribution of the ER during T cell activation

The experiment investigating the spatial distribution of the ER during T cell activation was carried out four times.

Experiment 1

Figure 28 shows two representative cells for every incubation time on activating and non-activating SLBs. In experiment 1, cells were incubated 2 min, 5 min and 10 min on activating SLBs and for 5 min on non-activating SLBs. The intensity of the images was scaled the same for every image. Comparing the ER signal after 5 and 15 min activation with 2 min and 5 min resting controls, clearly shows a brighter signal for the conditions with longer incubation times on activating SLBs.

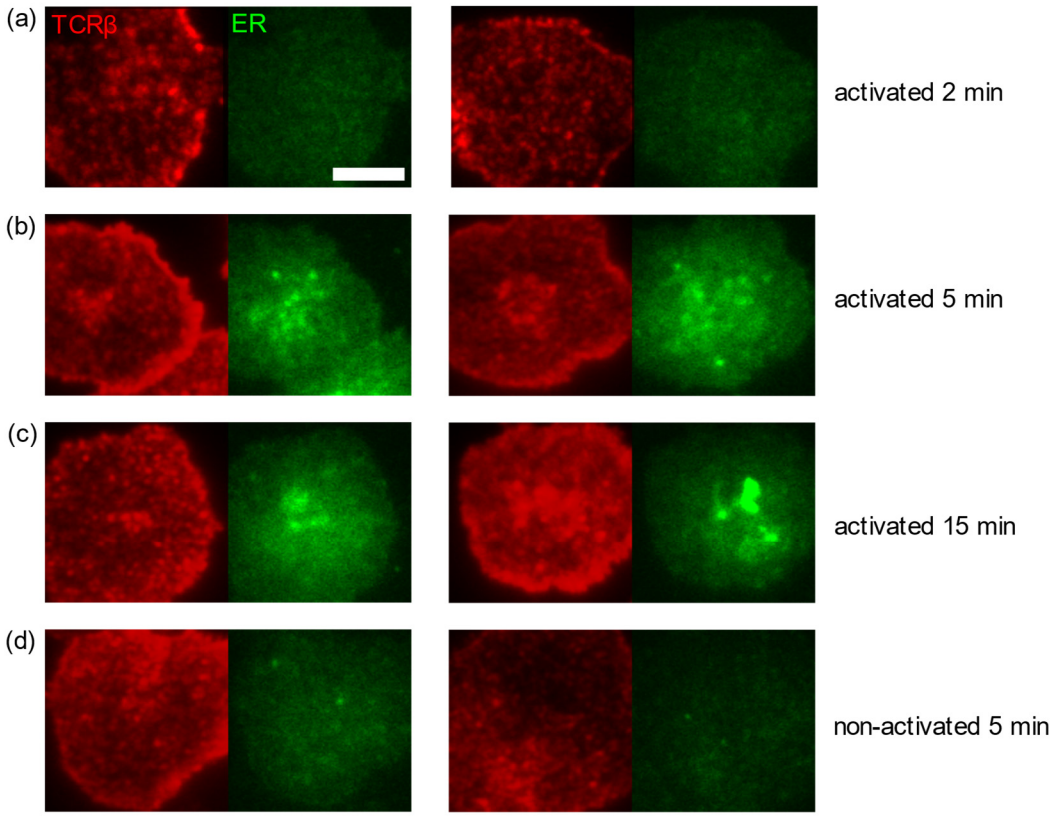

Figure 28: Representative images of the first TCR vs ER experiment. H57-AF647-labelled TCR is shown in red, Cytopainter-labelled ER is shown in green. For every condition two representative cells are shown. Panel a shows cells incubated 2 min on activating SLBs, b shows cells incubated 5 min on activating SLBs, c shows cells incubated 15 min on activating SLBs and d shows cells incubated for 5 min on non-activating SLBs. An increase in the ER signal for activated cells incubated for 5 min and 15 min can be seen in panels b and c. Scale bar: 5 µm

The results were also confirmed by boxplots for the mean gray value inside a specific ROI, the standard deviation of this gray value and the coefficient of variation, which are illustrated in **Figure 29**. All three values show a signal increase from the ER after 5 min and 15 min activation compared to 2 min activation. Intensity values after 5 min incubation on non-activating SLBs are at the same level as after 2 min incubation on activating SLBs.

Figure 29: Evaluation of the mean value per pixel, its standard deviation and the coefficient of variation for intensity (gray) values of the ER in a ROI excluding the boundaries of the cell. Data are represented in boxplots and separated by different activation times. Orange shaded boxes illustrate data of activated cells, blue shaded ones of non-activated cells. Mean gray value, standard deviation and coefficient of variation show an increase for 5 min and 15 min activated cells.

Experiment 2

The tendency of an increased signal in the ER channel described for the first experiment was confirmed in the second experiment (**Figure 30** and **Figure 31**). Here, a noticeable increase of the mean gray value, the standard deviation and the coefficient of variation was detected in cells incubated for 15 min on activating SLBs, compared to cells incubated only for 2 min or for 5 min on activating SLBs. In experiment 1, this effect was already visible for cells incubated 5 min at activating conditions. One reason could be that cells incubated for 5 min in experiment

2 only showed microcluster formation, while for cells in experiment 1 a c-SMAC could be detected. This would indicate a different activation stage of the T cells.

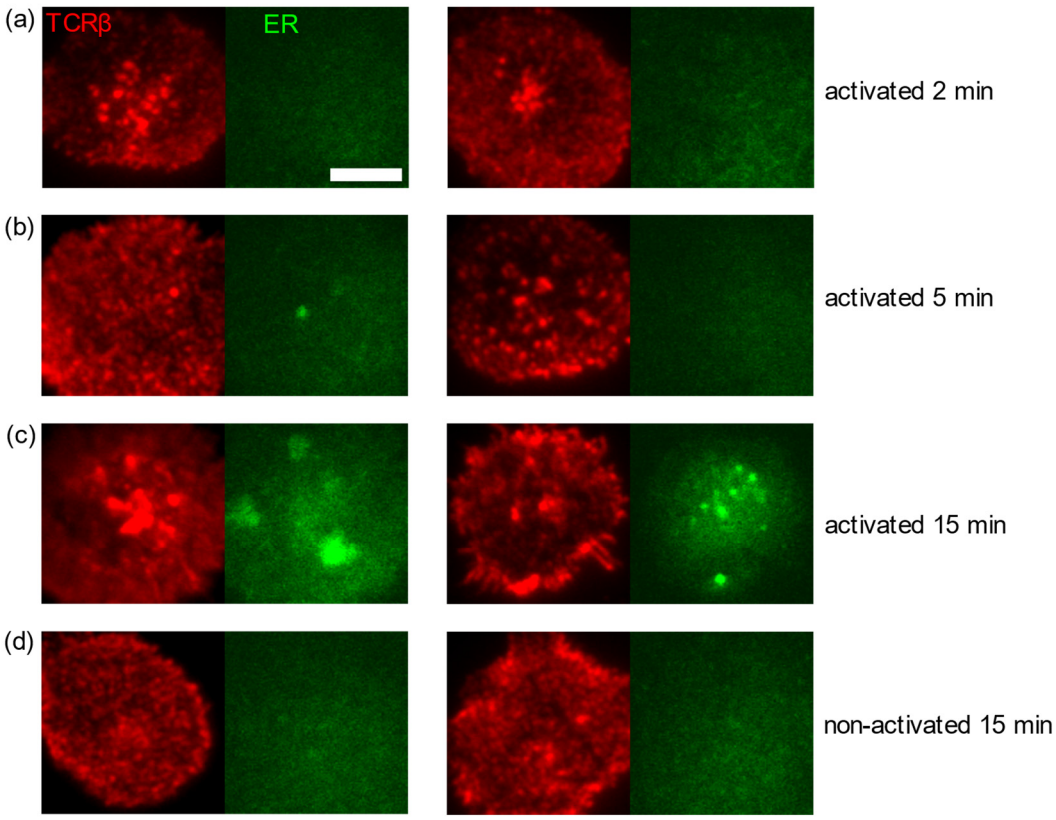

Figure 30: Representative images of the second TCR vs ER experiment. H57-AF647-labelled TCR is shown in red, Cytopainter-labelled ER is shown in green. For every condition, two representative cells are shown. Panel a shows cells incubated for 2 min on activating SLBs, b shows cells incubated for 5 min on activating SLBs, c shows cells incubated for 10 min on activating SLBs and d shows cells incubated for 15 min on non-activating SLBs. An increase in the ER signal for activated cells incubated for 15 min can be seen in panel c. Scale bar: 5 µm

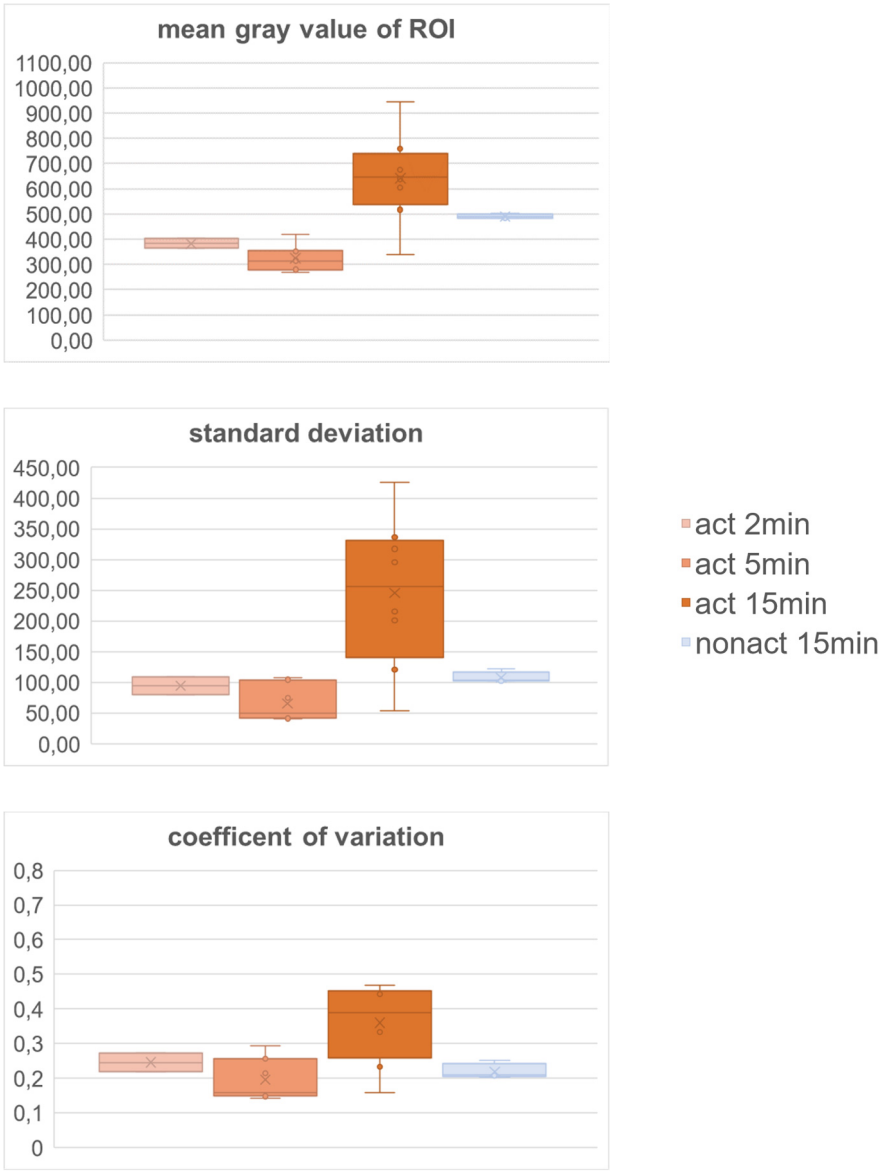

Figure 31: Evaluation of the mean gray value, its standard deviation and the coefficient of variation for intensity values of the ER in a ROI excluding the boundaries of the cell. Data is represented in boxplots and separated in different activation times. Orange shaded boxes illustrate data of activated cells, blue shaded ones of non-activated cells. All parameters show a time-dependent increase after incubation for 15min on activating SLBs.

Experiment 3

Representative images of cells of the third experiment are shown in **Figure 32**. The results show a high amount of intra- and extracellular background for all incubation conditions, except for cells incubated for 2 min on non-activating SLBs. A prominent increase of the ER signal due to activation as in experiment 1 and 2 was not detectable.

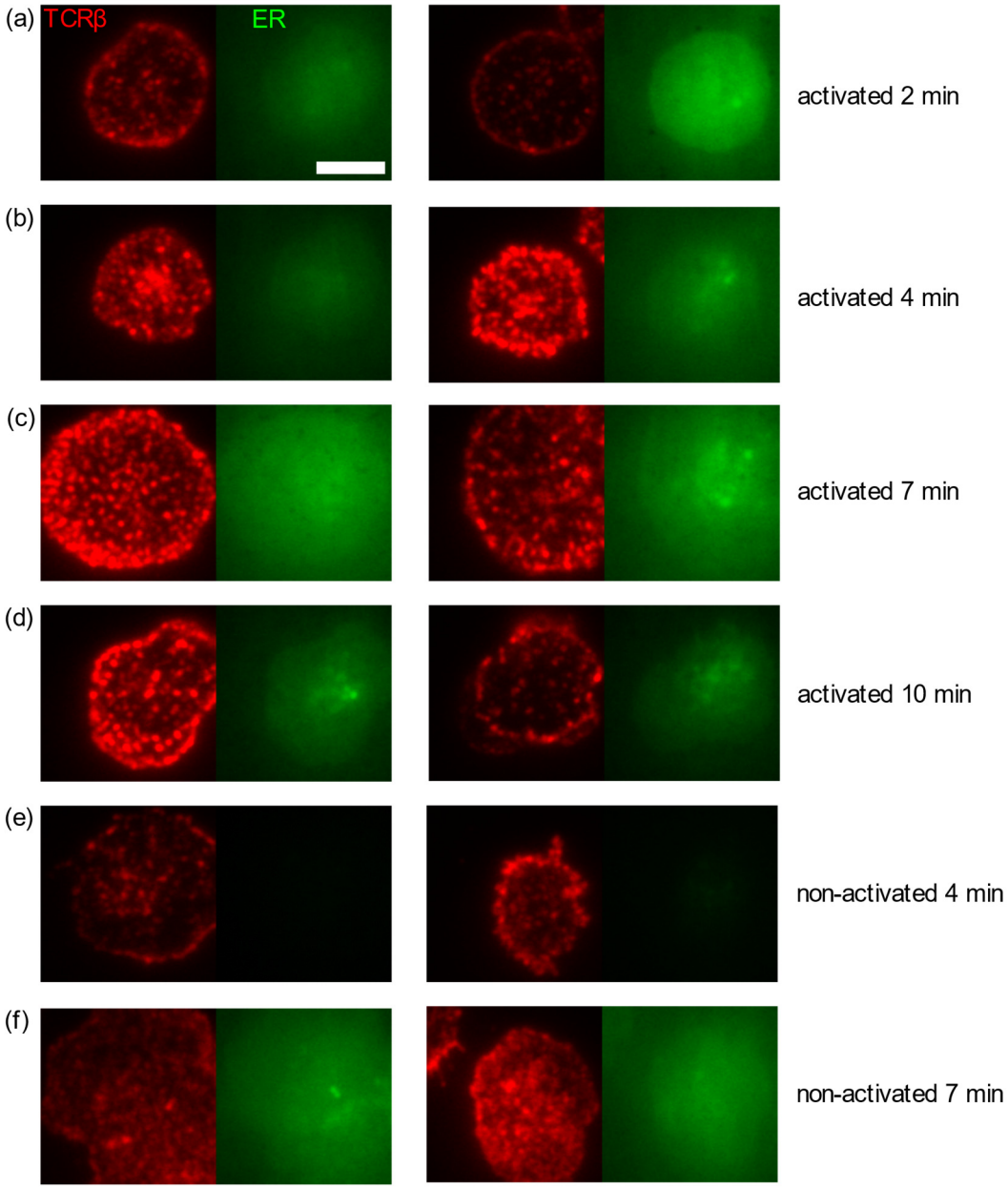

Figure 32: Representative images of the third TCR vs ER experiment. H57-AF647-labelled TCR is shown in red, Cytopainter-labelled ER is shown in green. For every condition two representative cells are shown. Panel a shows cells incubated 2 min on activating SLB, b shows cells incubated 4 min on activating SLB, c shows cells incubated to for 7 min on activating SLB, d shows cells incubated 10 min on activating SLB, e shows cells incubated for 4 min on non-activating SLB and f shows cells incubated for 7 min on non-activating SLB. Background signal in the ER channel is very high which makes the comparison of ER signal intensities between activated and non-activated cell difficult. The typical increased signal ER signal pattern as shown in experiment 1 and experiment 2 were not detectable. Scale bar: 5 µm

Figure 33 shows the evaluation of the calculated parameters for experiment 3. In this figure the mean gray value is increased when comparing for example 4 min activated and 2 min activated, but there is an increase between the two non-activating conditions as well. Boxplots for the coefficient of variation show no significant differences between all six tested conditions.

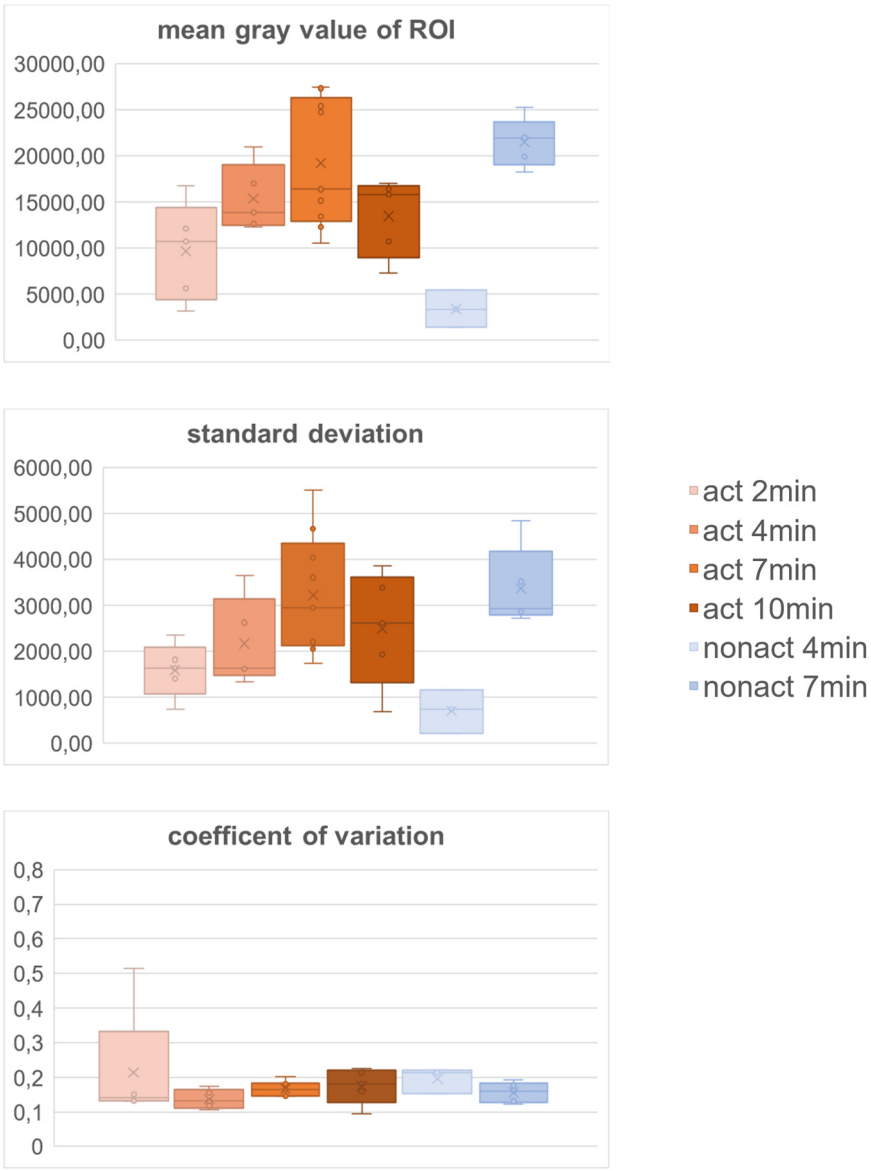

Figure 33: Evaluation of the mean gray value, its standard deviation and the coefficient of variation for pixel values of the ER signal in a ROI excluding the boundaries of the cell. Data is represented in boxplots and separated in different activation times. Orange shaded boxes illustrate data from activated cells, blue shaded boxes those of non-activated cells.

Experiment 4

In this experiment the number of conditions was increased again to get a higher time resolution of the T cell activation process. However, as seen in the results of experiment 3, also in this experiment the background signal of the ER channel inside and outside of the cells was very bright. Representative images of cells in **Figure 34** show no difference for activating and non-activating conditions. Bright spots emitted by the fluorophore bound to the ER are not visible upon T cell activation.

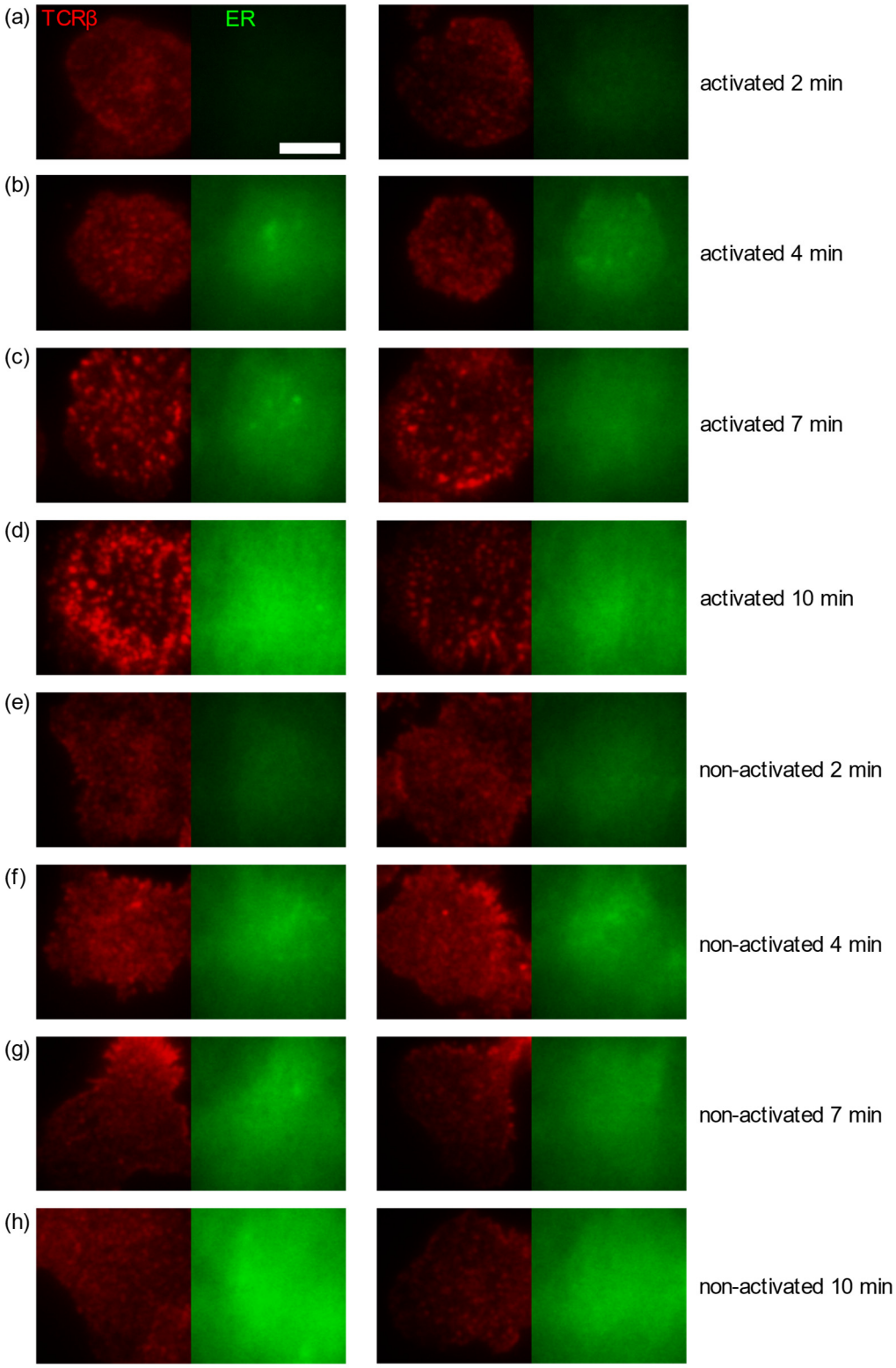

Figure 34: Representative images of the fourth TCR vs ER experiment. H57-AF647-labelled TCR is shown in red, Cytopainter-labelled ER is shown in green. For every condition two representative cells are shown. Panel a shows cells incubated 2 min on activating SLB, b shows cells incubated 4 min on activating SLB, c shows cells incubated to for 7 min on activating SLB, d shows cells incubated 10 min on activating SLB, e shows cells incubated for 2 min on non-activating SLB, f shows cells incubated for 4 min on non-activating SLB, g shows cells incubated for 7 min on non-activating SLB and h shows cells incubated for 10 min on non-activating SLB. Background signal is very bright for all conditions and a difference between activated and non-activated cells is not detectable. Scale bar: 5 µm

Figure 35 shows boxplots of the evaluated parameters for cells from experiment 4. An increase of the mean gray values and the standard deviation for cells incubated for 4, 7 and 10 min on activating SLB compared to cells incubated for only 2 min was recorded. This increase cannot be explained by a higher ER signal due to binding to the plasma membrane, as there is no typical fluorescence pattern visible (**Figure 34**). In addition, the same trend in signal increase is seen for non-activated cells incubated for a longer time on the SLB.

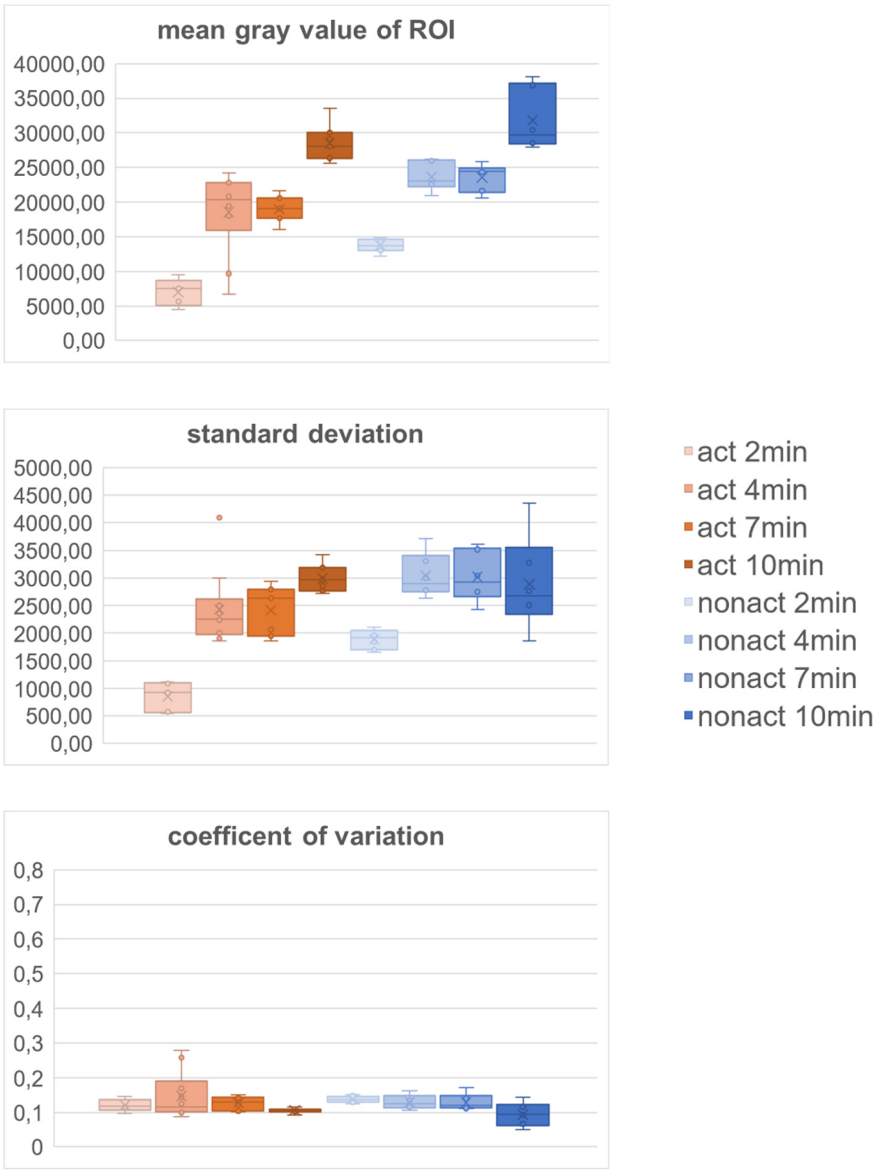

Figure 35: Evaluation of the mean gray value, its standard deviation and the coefficient of variation for pixel values of the ER in a ROI excluding the boundaries of the cell. Data is represented in boxplots and separated in different activation times. Orange shaded boxes illustrate data of activated cells, blue shaded ones of non-activated cells.

Figure 36a shows two cells of experiment 1 and experiment 2 where the TCR and ER channels were overlaid to judge the spatial distribution of these two structures. The two images suggest that the ER and the TCR might spatially exclude each other. Therefore, the spatial distribution of these two structures might affect each other. To validate this information, intensity profiles of the red and blue channels are illustrated in **Figure 36b**. The intensity profiles were evaluated horizontally within the ROI indicated by a yellow box shown in **Figure 36a**. For every vertical position within the ROI, one intensity profile was generated. For the resulting curve in **Figure 36b** these intensity profiles were averaged. For better comparability the intensity values of the two channels were normalized. The intensity profile of the left cell shows different positions for the maxima of the normalized intensity. Compared to the left cell, the right cell shows a different result. Intensity maxima in the red channel (TCR) are identifiable in the intensity profile as well as in the marked ROI in **Figure 36a**. The green channel (ER), on the other hand, shows a more homogeneous signal along the chosen ROI.

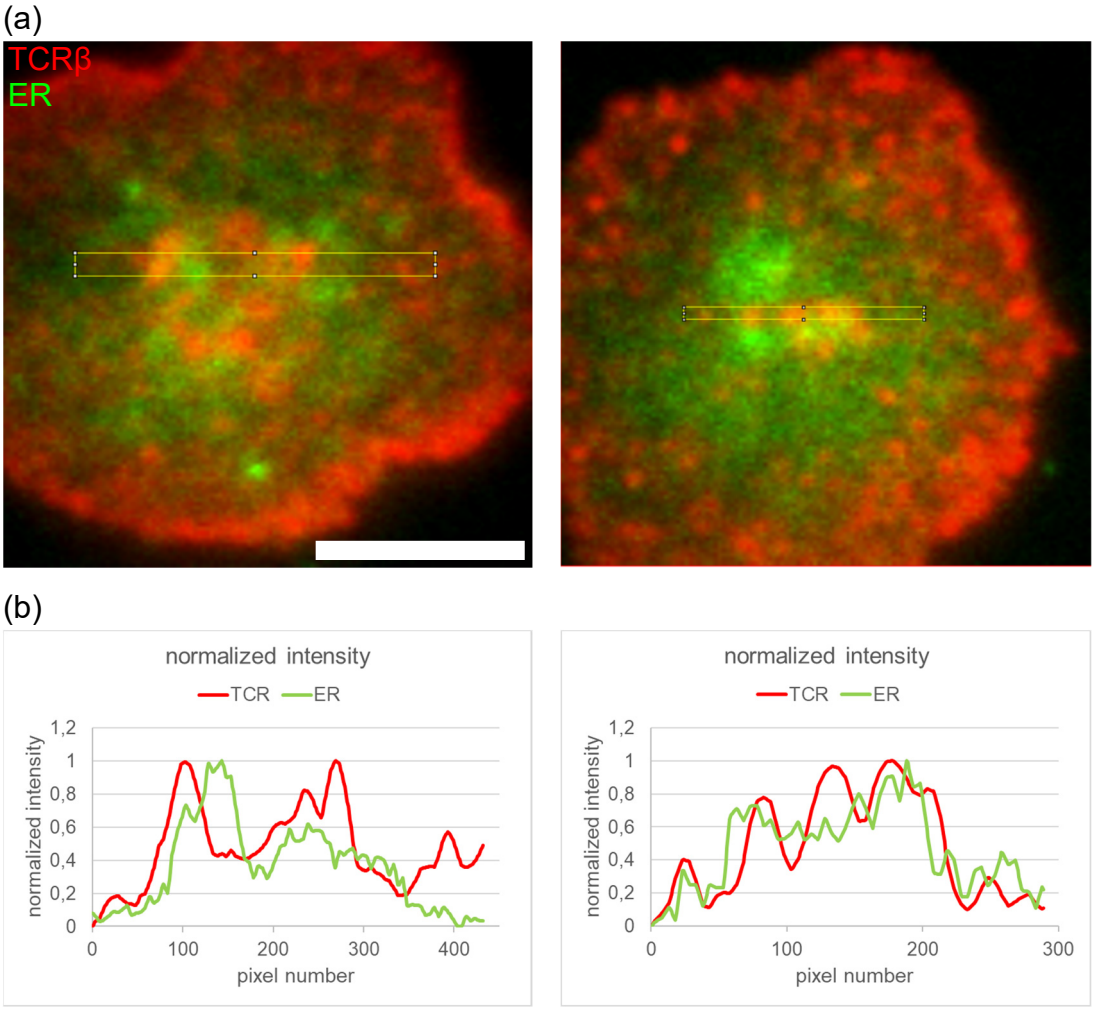

Figure 36: Images of the TCR signal (red) overlaid with the signal of the ER (green) (a) to judge if the position of the TCR is restricted by the spatial distribution of the ER or vice versa. In panel b intensity profiles were evaluated horizontally for the yellow marked ROI in panel a. Scale bar: 5 µm.

4. Discussion

4.1. Cluster analysis by two-color dSTORM measurements

In the presented Master project, a novel approach using two-color dSTORM measurements in combination with the cumulative density function of nearest-neighbor-distances between the two color channels was tested for artifact-free cluster detection. The method was used in activated and non-activated primary murine T cells. According to the work of Magdalena Schneider [7], the method should be capable to detect real nanoclustering without detecting clusters, which appear due to imaging artifacts like fluorophore blinking. In the presented work, the method should be used to confirm the findings by Rossboth et al. [33], who found that the TCR is not located in nanoclusters in non-activated T cells. On the other hand, in activated T cells, the method should detect microclusters, which form upon T cell activation and can also be seen in diffraction-limited fluorescence microscopy images. The experiment was carried out seven times. However, only data of the last experiment was good enough to perform the two-color dSTORM cluster analysis described in chapter 2.6. As shown in **Figure 20**, there were only very few localizations detected in the red channel (TCR labeled with H57-AF647) in the first six experiments. Looking at the original image sequences, revealed that the fluorophores did not blink in the red channel. Instead, the number of signals decreased, probably because of fluorophore bleaching within the first ~2000 frames. Unfortunately, this problem could not be solved in experiments 2 to 6. First, we speculated that the adjustment of the microscope setup may have led to the problem. However, measurements of the laser power revealed no problem in terms of the lasers. Next, we tried to change the reagents of the two-color dSTORM buffer. To use of dyes of different structure, like AF647 in combination with AF488 can be challenging, because their requirements for the STORM imaging buffer are different. Nahidiazar et al. [20] developed a so-called OXEA buffer system, which works well for two-color dSTORM measurements. We first prepared a new batch of cysteamine at pH 8.0 – 8.5. This, however, did not solved the problem. Also, the use of fresh OxyFluor reagent did not improve the data. Lastly, a new H57-AF647 antibody was ordered and used for experiment 7. This finally solved the experimental problems. **Figure 21** illustrates a much more similar localization density in the red and the blue channels. One reason for this problem could have been the reduced integrity of the antibody, which would lead to decreased labelling of the TCR. For example, wrong handling in respect of cooling could be an issue. Another problem found

during analysis was the use of the same intensity threshold for fitting the blue and the red channels with ThunderStorm. This issue was already known form empirical tests previous to this thesis. Using the same thresholds for both channels, leads to great numbers of spurious localizations detected in the blue channel. Many of them were also outside of the cell. Therefore, different thresholds were tested for the blue channel. Usually, dynamic thresholding was used. Fixed thresholds also work fine, but can also have the disadvantage of not being flexible enough if the images are heterogenous in terms of background and signal intensities. Threshold 2*std or 2.5*std of the first level of the used wavelet filter (for further details on the used parameters see **Table 1** to **Table 3** in chapter 2.5.1) worked fine for the blue channel for activated and non-activated cells. Looking at the results illustrated in **Figure 22**,**Figure 24**,**Figure 25** and**Figure 26**, a clear difference in the p-value distribution for non-activated and activated T cells can be appreciated, which does not depend on the chosen thresholds. p-values of activated cells are below the significance level of 0.05 in most cases. This suggests a rejection of H_0 and therefore a non-random distribution of molecules. This result was clearly expected due to the fact that the method should be able to detect nanocluster and T cells form TCR microclusters upon T cell activation. These microclusters could be clearly seen in the original data and within the localization maps. According to Rossboth et al. [33], the TCR is not organized in nanoclusters in non-activated T cells. For the two-color cluster detection method, this would mean a uniform p-value distribution for non-activated T cells. While p-value distribution for non-activated T cells shows a clear difference compared to activated cells, the distributions are overall not completely uniform and show a slight shift to small p-values. This would indicate non-random emitter distribution for some cells. The observation of a non-uniform p-value distributions for random protein distributions was also made by Magdalena Schneider for experiments in HeLa cells. In case of the presented thesis, we found a more uniform distribution when generating the toroidal shift models for localizations detected in the red channel. Additionally, there was a slight difference if excluding 2000 or 3000 frames at the beginning of the movies, see **Figure 25** and **Figure 26**. However, using less frames could lead to too few localizations for analysis. On the other hand, excluding more frames decreases the risk of emitters not separated sufficiently and decreases the cytosolic background signal due to bleaching. Such background signals, which are constantly detected, could lead to false positives in cluster analysis and should be avoided. If the signal to noise ratio is a problem in further experiments, it should be taken into consideration to use again a high-power laser illumination prior to imaging instead of directly recording and excluding frames during analysis. This could have the advantage, that the laser pulse prior to the imaging sequence can

be done in non-TIR configuration and therefore reduce also background signals coming from cytosolic structures.

4.2. Spatial distribution of the ER during T cell activation

In these experiments the spatial distribution of the ER during the activation process of primary murine T cells was investigated. According to Hogan et al. [25], STIM1, which is located in the ER membrane, binds to CRAC channels placed in the cell plasma membrane during the signaling cascade upon T cell activation. In theory this can bring the ER in close proximity to the plasma membrane. The TCR and the ER were stained simultaneously and measurements were conducted to show if the quantity of ER near to the plasma membrane changes upon T cell activation. Staining of the TCR allowed to judge if the T cells were activated and additionally revealed whether the position of the ER influences the spatial distribution of the TCR or *vice versa*. The data quality was not ideal in all measurements. The high background signal in the ER channel seen in **Figure 32** and **Figure 34** was already present in test measurements conducted previously to experiment 1 and experiment 2. A decrease in the incubation time and a decrease in the labeling concentration did not improve the data. After the drastic increase in data quality in experiments 1 and 2, the additional washing steps introduced after ER staining seemed to have helped. However, the high background signal was again visible in experiments 3 and 4, in spite of the additional washing steps. For these two experiments, the data quality was too bad to interpret the results. Looking at the cells of experiments 1 and 2 there is a visible increase of the ER signal upon T cell activation at specific points of the bottom of the cell. In experiment 1 this increase is already visible for cells incubated for 5 min on SLBs. In experiment 2, this increase is seen for cells incubated for 15 min. For cells incubated on non-activating SLBs, this signal increase is not seen. This qualitative judgment of images in **Figure 28 andFigure 30** can be confirmed by the parameters evaluated and visualized in boxplots for the different incubation conditions (**Figure 29 and Figure 31**). Upon T cell activation, an increase of the mean gray value of the ER channel, its standard deviation and also of the coefficient of variance is shown. This means that there is an increased portion of ER at some points near to the plasma membrane. To get information about the colocalization of the two structures, data of better quality would be necessary. Another problem of the ER Cytopainter staining kit is, that it is not stated to which structure of the ER the fluorophore binds. This makes colocalization interpretations very difficult, because a signal

emitted from parts of the ER really close to the plasma membrane but without a real connection to it, can be detected and would lead to a false positive result. This could mean that parts of the ER are detected, but do not influence the spatial distribution of the TCR. Nevertheless, images as shown in **Figure 36** could encourage the idea that TCR positions are restricted by the binding of the ER to the plasma membrane, or *vice versa*. In order to better interpret these results, an antibody directly binding to STIM1 in the ER membrane would be useful. Another method would be to use the construct developed by Chang et al. [48] which is called MAPPER. MAPPER is a genetically encoded marker that allows for direct imaging junctions between the ER and the plasma membrane. MAPPER was tested in HeLa cells by analyzing the colocalization with the ER and with STIM1 and the dynamics of the junctions by changing the amount of cytosolic Ca^{2+}. They state that MAPPER makes imaging of the ER plasma membrane junctions possible without affecting their size, their density, their gap distance and their function. Ectopic expression of MAPPER in primary mouse T cells could help to directly image the number of junctions upon activation and using two-color STORM measurements could facilitate colocalization studies between these two structures at the nanoscale. In addition, future measurements could be conducted with live cells in combination with Ca^{2+} influx measurements. This would allow to characterize the process of T cell activation in more detail and go beyond the method presented in this thesis.

References

[1] B. Alberts *et al.*, "Visualizing Cells," in *Molecular Biology of the Cell*, 6th ed., New York: Garland Science, 2015, pp. 529–564.

[2] U. Kubitscheck, Ed., *Fluorescence Microscopy*. Weinheim, Germany: Wiley-VCH Verlag GmbH & Co. KGaA, 2017.

[3] L. Schermelleh, R. Heintzmann, and H. Leonhardt, "A guide to super-resolution fluorescence microscopy," *J. Cell Biol.*, vol. 190, no. 2, pp. 165–175, Jul. 2010.

[4] M. F. Garcia-Parajo, A. Cambi, J. A. Torreno-Pina, N. Thompson, and K. Jacobson, "Nanoclustering as a dominant feature of plasma membrane organization.," *J. Cell Sci.*, vol. 127, no. Pt 23, pp. 4995–5005, Dec. 2014.

[5] A. Burgert, S. Letschert, S. Doose, and M. Sauer, "Artifacts in single-molecule localization microscopy.," *Histochem. Cell Biol.*, vol. 144, no. 2, pp. 123–31, Aug. 2015.

[6] F. Baumgart *et al.*, "Varying label density allows artifact-free analysis of membrane-protein nanoclusters," *Nat. Methods*, vol. 13, no. 8, pp. 661–664, Jun. 2016.

[7] M. Schneider, "Overcomming Blinking Artifacts in Nanocluster Detection Using Two-Color Single-Molecule Microscopy," Technical University of Vienna, 2018.

[8] K. Thorn, "A quick guide to light microscopy in cell biology.," *Mol. Biol. Cell*, vol. 27, no. 2, pp. 219–22, Jan. 2016.

[9] W. Demtröder, "Optische Instrumente," in *Experimentalphysik 2*, 6th ed., Springer Berlin Heidelberg.

[10] J. W. Lichtman and J.-A. Conchello, "Fluorescence microscopy.," *Nat. Methods*, vol. 2, no. 12, pp. 910–9, Dec. 2005.

[11] M. J. Rust, M. Bates, and X. Zhuang, "Sub-diffraction-limit imaging by stochastic optical reconstruction microscopy (STORM)," *Nat. Methods*, vol. 3, no. 10, pp. 793–796, Oct. 2006.

[12] S. van de Linde *et al.*, "Direct stochastic optical reconstruction microscopy with standard fluorescent probes," *Nat. Protoc.*, vol. 6, no. 7, pp. 991–1009, Jun. 2011.

[13] P. J. Goodhew, *Electron microscopy and analysis / P. J. Goodhew*. London : New York: Wykeham Publications ; Springer-Verlag, 1975.

[14] B. O. Leung and K. C. Chou, "Review of Super-Resolution Fluorescence Microscopy for Biology," *Appl. Spectrosc.*, vol. 65, no. 9, pp. 967–980, Sep. 2011.

[15] M. G. Gustafsson, "Surpassing the lateral resolution limit by a factor of two using structured illumination microscopy.," *J. Microsc.*, vol. 198, no. Pt 2, pp. 82–7, May 2000.

[16] S. W. Hell and J. Wichmann, "Breaking the diffraction resolution limit by stimulated emission: stimulated-emission-depletion fluorescence microscopy," *Opt. Lett.*, vol. 19, no. 11, pp. 780–782, 1994.

[17] E. Betzig *et al.*, "Imaging Intracellular Fluorescent Proteins at Nanometer Resolution," *Science (80-.).*, vol. 313, no. 5793, p. 1642 LP-1645, Sep. 2006.

[18] M. Heilemann *et al.*, "Subdiffraction-Resolution Fluorescence Imaging with Conventional Fluorescent Probes," *Angew. Chemie Int. Ed.*, vol. 47, no. 33, pp. 6172–6176, Jul. 2008.

[19] J. Tam, G. A. Cordier, J. S. Borbely, Á. Sandoval Álvarez, and M. Lakadamyali, "Cross-Talk-Free Multi-Color STORM Imaging Using a Single Fluorophore," *PLoS One*, vol. 9, no. 7, p. e101772, Jul. 2014.

[20] L. Nahidiazar, A. V Agronskaia, J. Broertjes, B. van den Broek, and K. Jalink, "Optimizing Imaging Conditions for Demanding Multi-Color Super Resolution

Localization Microscopy," *PLoS One*, vol. 11, no. 7, p. e0158884, Jul. 2016.
[21] K. N. Fish, "Total Internal Reflection Fluorescence (TIRF) Microscopy," *Curr. Protoc. Cytom.*, Oct. 2009.
[22] H. Schneckenburger, "Total internal reflection fluorescence microscopy: technical innovations and novel applications.," *Curr. Opin. Biotechnol.*, vol. 16, no. 1, pp. 13–8, Feb. 2005.
[23] B. Alberts *et al.*, "The Innate and Adaptive Immune System," in *Molecular Biology of the Cell*, 6th ed., New York: Garland Science, 2015, pp. 1297–1340.
[24] K. Murphy, P. Travers, M. Walport, and C. Janeway, *Janeway's immunobiology*. New York: Garland Science, 2012.
[25] P. G. Hogan, R. S. Lewis, and A. Rao, "Molecular basis of calcium signaling in lymphocytes: STIM and ORAI.," *Annu. Rev. Immunol.*, vol. 28, pp. 491–533, 2010.
[26] K. Simons and G. van Meer, "Lipid sorting in epithelial cells.," *Biochemistry*, vol. 27, no. 17, pp. 6197–202, Aug. 1988.
[27] T. Yokosuka *et al.*, "Newly generated T cell receptor microclusters initiate and sustain T cell activation by recruitment of Zap70 and SLP-76," *Nat. Immunol.*, vol. 6, p. 1253, Nov. 2005.
[28] B. F. Lillemeier, M. A. Mörtelmaier, M. B. Forstner, J. B. Huppa, J. T. Groves, and M. M. Davis, "TCR and Lat are expressed on separate protein islands on T cell membranes and concatenate during activation," *Nat. Immunol.*, vol. 11, p. 90, Dec. 2009.
[29] Y. S. Hu, H. Cang, and B. F. Lillemeier, "Superresolution imaging reveals nanometer- and micrometer-scale spatial distributions of T-cell receptors in lymph nodes," *Proc. Natl. Acad. Sci.*, vol. 113, no. 26, p. 7201 LP-7206, Jun. 2016.
[30] R. Kumar *et al.*, "Increased Sensitivity of Antigen-Experienced T Cells through the Enrichment of Oligomeric T Cell Receptor Complexes," *Immunity*, vol. 35, no. 3, pp. 375–387, 2011.
[31] S. V Pageon *et al.*, "Functional role of T-cell receptor nanoclusters in signal initiation and antigen discrimination," *Proc. Natl. Acad. Sci. U. S. A.*, vol. 113, no. 37, pp. E5454–E5463, Sep. 2016.
[32] K.-H. Roh, B. F. Lillemeier, F. Wang, and M. M. Davis, "The coreceptor CD4 is expressed in distinct nanoclusters and does not colocalize with T-cell receptor and active protein tyrosine kinase p56lck," *Proc. Natl. Acad. Sci. U. S. A.*, vol. 112, no. 13, pp. E1604–E1613, Mar. 2015.
[33] B. Rossboth *et al.*, "TCRs are randomly distributed on the plasma membrane of resting antigen-experienced T cells," *Nat. Immunol.*, vol. 19, no. 8, pp. 821–827, 2018.
[34] P. Annibale, S. Vanni, M. Scarselli, U. Rothlisberger, and A. Radenovic, "Identification of clustering artifacts in photoactivated localization microscopy.," *Nat. Methods*, vol. 8, no. 7, pp. 527–8, Jun. 2011.
[35] D. R. Whelan and T. D. M. Bell, "Image artifacts in Single Molecule Localization Microscopy: why optimization of sample preparation protocols matters," *Sci. Rep.*, vol. 5, no. 1, p. 7924, Jul. 2015.
[36] F. Baumgart *et al.*, "Varying label density allows artifact-free analysis of membrane-protein nanoclusters," *Nat. Methods*, vol. 13, no. 8, pp. 661–664, Aug. 2016.
[37] G. K. Voeltz, M. M. Rolls, and T. A. Rapoport, "Structural organization of the endoplasmic reticulum," *EMBO Rep.*, vol. 3, no. 10, pp. 944–950, Oct. 2002.
[38] D. S. Schwarz and M. D. Blower, "The endoplasmic reticulum: structure, function and response to cellular signaling," *Cell. Mol. Life Sci.*, vol. 73, no. 1, pp. 79–94, 2016.
[39] J. B. Huppa, M. Gleimer, C. Sumen, and M. M. Davis, "Continuous T cell receptor signaling required for synapse maintenance and full effector potential.," *Nat.*

Immunol., vol. 4, no. 8, pp. 749–55, Aug. 2003.
[40] R. P. Richter, R. Bérat, and A. R. Brisson, "Formation of Solid-Supported Lipid Bilayers: An Integrated View," *Langmuir*, vol. 22, no. 8, pp. 3497–3505, Apr. 2006.
[41] C. Yu and J. T. Groves, "Engineering supported membranes for cell biology," *Med. Biol. Eng. Comput.*, vol. 48, no. 10, pp. 955–963, 2010.
[42] BioLegend Inc, "Alexa Fluor® 647 anti-mouse TCR β chain Antibody," 2014. [Online]. Available: https://www.biolegend.com/en-us/global-elements/pdf-popup/alexa-fluor-647-anti-mouse-tcr-beta-chain-antibody-3272?filename=Alexa Fluor 647 anti-mouse TCR beta chain Antibody.pdf&pdfgen=true. [Accessed: 03-Nov-2018].
[43] BioLegend Inc, "Alexa Fluor® 488 anti-mouse TCR β chain Antibody," 2014. [Online]. Available: https://www.biolegend.com/en-us/global-elements/pdf-popup/alexa-fluor-488-anti-mouse-tcr-beta-chain-antibody-2713?filename=Alexa Fluor 488 anti-mouse TCR beta chain Antibody.pdf&pdfgen=true. [Accessed: 03-Nov-2018].
[44] Abcam, "CytoPainter ER Staining Kit – Green Fluorescence," 2012. [Online]. Available: https://www.abcam.com/ps/products/139/ab139481/documents/ab139481 CytoPainter ER Staining kit Green Fluorescence (website).pdf. [Accessed: 03-Nov-2018].
[45] J. Schindelin *et al.*, "Fiji: an open-source platform for biological-image analysis," *Nat. Methods*, vol. 9, no. 7, pp. 676–682, Jul. 2012.
[46] M. Ovesný, P. Křížek, J. Borkovec, Z. Svindrych, and G. M. Hagen, "ThunderSTORM: a comprehensive ImageJ plug-in for PALM and STORM data analysis and super-resolution imaging.," *Bioinformatics*, vol. 30, no. 16, pp. 2389–90, Aug. 2014.
[47] H. W. Lotwick and B. W. Silverman, "Methods for Analysing Spatial Processes of Several Types of Points," *J. R. Stat. Soc. Ser. B*, vol. 44, no. 3, pp. 406–413, 1982.
[48] C.-L. Chang *et al.*, "Feedback Regulation of Receptor-Induced Ca2+ Signaling Mediated by E-Syt1 and Nir2 at Endoplasmic Reticulum-Plasma Membrane Junctions," *Cell Rep.*, vol. 5, no. 3, pp. 813–825, 2013.

Eidesstattliche Erklärung

Hiermit erkläre ich, dass die vorliegende Arbeit gemäß dem Code of Conduct – Regeln zur Sicherung guter wissenschaftlicher Praxis, insbesondere ohne unzulässige Hilfe Dritter und ohne Benutzung anderer als der angegebenen Hilfsmittel, angefertigt wurde. Die aus anderen Quellen direkt oder indirekt übernommenen Daten und Konzepte sind unter Angabe der Quelle gekennzeichnet. Die Arbeit wurde bisher weder im In– noch im Ausland in gleicher oder in ähnlicher Form in anderen Prüfungsverfahren vorgelegt.

Wien, 28.11.2018

.....

Bernd Reutterer